Corotating Interaction Regions and Interplanetary Sheaths during Solar Cycle 24: A Comparative Study on Their Characteristics and Geoeffectiveness

M.Sc. Thesis

By

Jibin V. Sunny

DISCIPLINE OF ASTRONOMY, ASTROPHYSICS AND SPACE ENGINEERING

INDIAN INSTITUTE OF TECHNOLOGY INDORE

MAY 2022

Corotating Interaction Regions and Interplanetary Sheaths during Solar Cycle 24: A Comparative Study on Their Characteristics and Geoeffectiveness

A THESIS

Submitted in partial fulfillment of the requirements for the award of the degree
of
Master of Science

by
Jibin V. Sunny

DISCIPLINE OF ASTRONOMY, ASTROPHYSICS AND SPACE ENGINEERING
INDIAN INSTITUTE OF TECHNOLOGY INDORE

MAY 2022

INDIAN INSTITUTE OF TECHNOLOGY INDORE

CANDIDATE'S DECLARATION

I hereby certify that the work which is being presented in the thesis entitled **"Corotating Interaction Regions and Interplanetary Sheaths During Solar Cycle 24: A Comparative Study on Their Characteristics and Geoeffectiveness"** in the partial fulfillment of the requirements for the award of the degree of **Master of Science** and submitted in the **Discipline of Astronomy, Astrophysics and Space Engineering, Indian Institute of Technology Indore**, is an authentic record of my own work carried out during the time period from August 2022 to May 2022 under the supervision of Dr. Saurabh Das, Assistant Professor, IIT Indore and Dr. Rajkumar Hajra, Ramanujan Fellow, IIT Indore.

The matter presented in this thesis has not been submitted by me for the award of any other degree of this or any other institute.

23-05-2022

Signature of the student with date

(JIBIN V. SUNNY)

This is to certify that the above statement made by the candidate is correct to the best of my/our knowledge.

S. Das 23/05/2022
Signature of the Supervisor of
M.Sc. thesis #1 (with date)
(DR. SAURABH DAS)

Rajkumar Hajra 23-05-2022
Signature of the Supervisor of
M.Sc. thesis #2 (with date)
(DR. RAJKUMAR HAJRA)

Jibin V. Sunny has successfully given his/her M.Sc. Oral Examination held on **06 May 2022**.

Signature of PSPC Member #1
Date: 23-05-2022

Saptarshi Ghosh
Signature of PSPC Member #2
Date: 23-05-2022

Signature of PSPC Member #3
Date:

S. Das Rajkumar Hajra
Signature(s) of Supervisor(s).
Date: 23-05-2022

Signature of M.Sc. Co-Ordinator
Date: 25-05-2022

S. Das 23/05/2022
Convener, DPGC
Date:

Manoneeta Chakraborty
Signature of HoD (Officiating)
Date: 26/05/2022

ACKNOWLEDGEMENT

I would like to thank my supervisors, Dr. Rajkumar Hajra and Dr. Saurabh Das, for their invaluable supervision, guidance, support and tutelage during the course of my M.Sc. Thesis work. The guidance and advices shared by Dr. Rajkumar Hajra were beyond my expectation and they not only enlightened me with academic knowledge but also gave valuable advices whenever needed. Without such efficient supervision this work might not have happened. My gratitude extends to all the Faculties of Department of Astronomy, Astrophysics and Space Engineering, Indian Institute of Technology Indore for the opportunity to undertake my studies at the department.

I would also thank my parents Mr. Sunny T and Mrs. Mini Paul and my brother Mr. Jithin V Sunny for their valuable support and love. Additionally, I would like to express gratitude to all my colleagues and friends for their treasured support which was really influential in shaping my experiment methods and critiquing my results. I also thank Mr. Swaroop Georgy Zachariah for his encouragement and support.

I would like to mention Ankit India, Gursharanjith Kaur, Kishlay Singh, Kunal Motghare, Manish Singh, Priyankar Mukherjee, Pawan Tiwari, Sirsha Nandy and Sohini Dutta for all the care and love you all shared.

DEDICATION

This work is dedicated to my friend Priyankar Mukherjee (Priyan) who inspired me a lot.

Abstract

Space weather events are initiated on the Sun and can cause immense impacts on the Earth's magnetosphere-ionosphere-atmosphere system. The events cause geomagnetic storms which can damage the satellite communication, navigation and power grid system. Corotating interaction regions (CIRs) and interplanetary sheaths are two such events. A CIR is the interaction region between the high-speed solar stream emanated from coronal hole and the slow speed stream. Interplanetary sheaths are turbulent regions formed by fast moving interplanetary coronal mass ejections (ICMEs). In this work, I used a long-term solar-wind measurement upstream of the Earth during Solar Cycle 24, from January 2008 to December 2019, to identify all CIRs and sheaths, to compare their solar-cycle and seasonal variations, characteristic features and geoeffectiveness. A total of 290 CIRs and 110 sheaths were encountered by Earth during this period. Both sheath and CIR are characterized by identical average solar-wind plasma density and ram pressure, and their fluctuations characterized by enhanced variance, and periodic variations of a few minutes to an hour. However, on average, the CIRs are faster, hotter, durationally longer and radially wider than the sheaths. Also, on average CIRs has stronger southward interplanetary magnetic field (IMF) component than sheaths which makes the CIRs more geoeffective than the sheaths. Comparative studies are also conducted between geoeffective and non-geoeffective CIRs and sheaths. The typical characteristic solar-wind and geomagnetic activity parameters given in this work may be useful for modelling and prediction purposes.

LIST OF PUBLICATIONS

- Hajra, R., and **J. V. Sunny** (2022), Corotating Interaction Regions during Solar Cycle 24: A Study on Characteristics and Geoeffectiveness, Solar Physics, 297, 30. https://doi.org/10.1007/s11207-022-01962-1 (Impact Factor = 2.671)
- Hajra, R., **J. V. Sunny**, M. Babu, and A. G. Nair (2022), Interplanetary Sheaths and Corotating Interaction Regions: A Comparative Statistical Study on Characteristics and Geoeffectiveness (Accepted for publication in Solar Physics) (Impact Factor = 2.671).
- **Sunny, J. V.**, A. G. Nair, M. Babu, and R. Hajra (2022), A Comparative Study on Geoeffective and Non-Geoeffective CIRs (submitted to Solar Physics).

TABLE OF CONTENTS

LIST OF FIGURES

Figure Description	Page No.

geoeffective and non-geoeffective sheaths. Gray and empty histograms correspond to geoeffective and non-geoeffective sheaths, respectively. Downward arrows indicate mean values of the parameters for all geoeffective (gray) and non-geoeffective (black) sheaths

LIST OF TABLES

ACRONYMS

- AE: Auroral Electrojet
- AU: Astronomical Unit
- B_0: Interplanetary Magnetic Field Magnitude
- B_z: Southward Component Of IMF
- CIR: Corotating Interaction Region
- CME: Coronal Mass Ejection
- GSM: Geocentric Solar Magnetospheric (coordinate system)
- HSS: (solar wind) High-Speed Stream
- IMF: Interplanetary Magnetic Field
- ICME: Interplanetary Coronal Mass Ejection
- MC: Magnetic Cloud
- N_{sw}: Plasma Density of Solar Wind
- P_{sw}: Ram Pressure
- Sfu: Solar flux unit
- T_{sw}: Temperature of Solar Wind
- UT: Universal Time
- V_{sw}: Velocity of Solar Wind

Chapter 1

Introduction

1.1. Definition of Space Weather

Everything from variations in the Sun and solar wind to their effects on interplanetary space, Earth, and other solar system entities with varied magnetic and plasma properties is considered space weather (e.g., Echer et al., 2005; Hajra et al., 2020; Hajra et al., 2021, and references therein). These occurrences are closely linked to the 11-year "Schwabe" cycle (Schwabe, 1844), in which the Sun's activity rises and falls, from minimum to maximum and back to minimum.

The term space weather is almost related to the terrestrial weather of the atmosphere of Earth by conception but is quite different. It is a branch of space science which deals with the time varying conditions in the solar system. The term space weather was used first in 1950s and became common in 1990s. The space weather is influenced within the solar system by the solar wind and interplanetary magnetic field (IMF) which is carried by the solar wind plasma. Space weather is associated with different kinds of physical phenomena which includes geomagnetic storms and substorms, geomagnetically induced currents, aurora, energization of Van Allen radiation belts, magnetospheric ionospheric and atmospheric impacts and scintillation of satellite to ground radio signals and long-range radar signals.

The major space weather events are the Corotating interaction regions (CIRs) and the Coronal mass ejections (CMEs) which can compress the magnetosphere and cause geomagnetic storms. These space weather phenomena can cause severe impacts and damages to communication satellite systems, long distance transmission lines, weather satellite system which provide weather related information for forecasting such events and can expose passengers and aircraft crews to radiations. Space weather affects a substantial percentage of modern technical systems, from space communication satellites to ground-based power grids. These phenomena can also interfere the satellite systems like Global Positioning Satellite system (GPS) and with radio signals with which they are operating. So, space weather become a relevant topic to be studied for the smooth performance of our day-to-day life.

1.2. CIRs

Corotating interaction region (CIR) is a compressed solar-wind plasma and magnetic field region, forming between a slow (≈300 – 450 km s^{-1}) solar-wind and a high-speed (≈500 – 800 km s^{-1}) stream (HSS) emanated from a coronal hole on the Sun (Belcher and Davis, 1971; Siscoe, 1972; Krieger et al., 1973; Smith and Wolfe, 1976; Pizzo, 1978). As coronal holes are generally long-lived structures on the rotating Sun, an HSS and the resultant CIR "corotate" with the Sun. Thus, they can be identified in interplanetary space more than once at an interval of ≈ 27 days, which is the solar differential rotation period at the solar Equator to mid-latitude regions (Snyder et al., 1963; Sheeley et al., 1977).

The coronal hole emanated HSSs are characterized by Alfvén wave trains (Tsurutani et al., 2006) which are strongly compressed within the CIRs. The southward component of the Alfvén waves reconnects with the northward (dayside) geomagnetic fields (Dungey, 1961). Thus, the CIR/HSS can largely affect the magnetosphere-ionosphere-thermosphere system of the Earth. This is generally called the "geoeffectiveness" of the CIR. The major CIR/HSS impacts include: (1) a rapid loss of relativistic (MeV) electrons in the Earth's outer radiation belt due to magnetospheric compression by the ram pressure enhancement during the CIR (Tsurutani et al., 2016a), followed by an electron acceleration during the following HSS (Hajra et al., 2014a, 2015a,b; Tsurutani et al., 2016b; Hajra et, al., 2018; Hajra, 2021b), (2) an enhancement of the ring currents in the inner magnetosphere leading to recurrent geomagnetic storms of moderate intensity (Tsurutani et al., 1995, 2006; Alves et al., 2006; Chi et al., 2018), (3) initiation of high-intensity long-duration continuous auroral electrojet (AE) activities (HILDCAAs; Tsurutani and Gonzalez, 1987; Hajra et al., 2013), (4) expansion and heating of the topside ionosphere (Hajra et al., 2017), and (5) enhancements in thermospheric temperature and density (e.g. Lei et al., 2011; Gardner et al., 2012, and references therein).

1.3. Sheaths

Coronal mass ejection (CME) originates from the active region of the sun. They erupt from these regions and propagates faster in the interplanetary medium, which is termed as interplanetary CME (ICME). Morrison in 1954 proposed the ejection of plasma and magnetic field from the active regions of the sun. He called such ejects as 'magnetic clouds. Gold proposed that a magnetic cloud might be preceded by a shock wave. A fast forward shock can be formed at the leading edge of a coronal mass ejection if it moves rapidly enough through solar wind (Sheeley et al., 1983, 1985; Kilpua et al., 2017). The ICME is preceded by a piled-up solar wind or the interplanetary sheath (Kennel et al., 1985; Tsurutani and Lin, 1985; Tsurutani et al., 1988). The fast forward shock is formed at the sheath leading edge when the ICME speed exceeds the ambient solar wind speed (Landau and Lifshitz, 1960; Kennel et al., 1985; Tsurutani et al., 2011). The zone between the shock and the magnetic cloud was discovered by Burlag et al. (1981) as turbulent hot plasma compressed by shock and containing a highly fluctuating magnetic field. Sheath refers to the chaotic zone generated between the shock and the ICME (Kilpua et al., 2017).

Various observations in the interplanetary medium have been interpreted as the signatures of CMEs (Gosling, 1990 and references therein.). The main interplanetary signatures of CME include depression in temperatures of solar wind plasma electrons (Montgomery et al., 1974) and protons (Gosling et al., 1973) and low variance magnetic field enhancements (Burlaga et al., 1981; Gosling et al., 1987; Tranquille et al., 1987) that often includes smooth rotations of the magnetic field components in the so called 'magnetic cloud' (Klein and Burlaga, 1982; Lepping et al., 1990). During magnetic cloud the plasma beta (ratio of the plasma pressure to the magnetic pressure) will also be low (Burlaga et al., 1981; Gosling et al., 1987). Burlaga et al., 1981 defines magnetic cloud with a high magnetic field, low temperature and density, and with the rotation of the field vectors indicating a loop.

Wilson was the first to discover a link between CMEs and geomagnetic storms (1987). Wilson discovered that the southerly component of the magnetic field was the driving force behind the storms. Wilson (1987) discovered that the Dst index concurrently declines to a significant negative value with the commencement of a substantial and continuous southerly magnetic field in a superposed epoch study of 19 magnetic clouds. It's also worth noting that the storm's recovery began when the magnetic field began to shift northward. The findings matched the known relationship between geomagnetic disturbances and the interplanetary magnetic field's southerly component (Dungey 1961; Fairfield and Cahill Jr 1966). In the shock sheaths, a southward interplanetary field can also occur (Gonzalez and Tsurutani 1987; Gosling and McComas 1987). Sheaths are thus proven to be equally crucial in the formation of geomagnetic storms (Tsurutani et at. 1988). It was obvious by the late 1980s that the southern component of the magnetic field in interplanetary CMEs (ICMEs) and/or the shock sheath is directly responsible for severe geomagnetic storms (Wilson 1987; Gonzalez and Tsurutani 1987).

1.4. Review of Past Work

CIR is a well explored topic and studies has been going on with interesting results. With a varying heliocentric distance, the shape, size and characteristics of a CIR change significantly (see Richardson, 2018, for an excellent review on this topic). The CIR observations in the inner heliosphere have been made by the Helios 1 and 2, the Pioneer Venus Orbiter, the Parker Solar Probe, and the Solar Orbiter spacecraft (Richter and Luttrell, 1986; Jian, 2008; Jian et al., 2008a, b; Allen et al., 2020, 2021, and references therein). The near-Earth CIRs have been studied by several spacecraft including the Interplanetary Monitoring Platform (IMP), Geotail, Advanced Composition Explorer (ACE), and Wind (Belcher and Davis, 1971; Tsurutani et al., 1995, 2006; Jian et al., 2006; Echer et al., 2011; Grandin et al., 2019; Nakagawa et al., 2019; Hajra et al., 2020, and references therein). The CIR study in the outer heliosphere have used observations made by the Pioneer 10 and 11, Voyager 1 and 2, and Rosetta spacecraft (Gosling et al., 1976; Hundhausen and Gosling, 1976; Smith and Wolfe, 1976; Burlaga et al., 1984; Gazis et al., 1999; Jian et al., 2011; Hajra et al., 2018; Hajra, 2021a, and references therein). Based on these studies, it is inferred that the radial velocity transition between the slow and fast streams steepens, and the plasma and magnetic field compression along the CIR interface increases and becomes sharper with increasing radial distance. As a consequence, fast forward and fast reverse shocks form at the leading and trailing edges of a CIR, respectively, beyond ≈ 2 AU from the Sun (Gosling et al., 1976; Smith and Wolfe, 1976). At ≈ 1 AU, a CIR is typically characterized by gradually enhanced plasma density and magnetic field magnitude, and only rarely bounded by fast forward and reverse shocks (Belcher and Davis, 1971; Tsurutani et al., 1995; Jian et al., 2006).

ICME is a well explored topic and many studies has been performed on magnetic cloud as well, but studies regarding interplanetary sheaths are comparatively low. Loop or bubble-like structures behind interplanetary shocks have been suggested from the first ICME observations in 1970s (Hirshberg et al., 1970; Gosling et al., 1973). Gopalswamy (2016) describes about a more detailed review on ICMEs. Kilpua et al. (2017) has done a descriptive study on interplanetary shocks and sheaths. An extensive fleet of instruments and space missions have monitored the solar wind and its transient structures since the discovery. From mid 1990s the spacecrafts like Wind, ACE, SOHO and DSCOVR near the Lagrangian point 1 (L1) has provided continuous observations of near-Earth solar wind.

1.5. Problem Formulation

Enhanced plasma speed, ram pressure, and most importantly southward IMF components during the sheaths and CIRs are responsible for their significant impacts on the inner magnetospheric ring current (Tsurutani et al., 1988, 1995; Huttunen et al., 2002; Huttunen and Koskinen, 2004; Tsurutani et al., 2006; Alves et al., 2006; Echer et al., 2008; Chiet al., 2018), radiation belt relativistic electrons (Hajra et al., 2014a, 2015a,b; Hajra et al., 2020; Tsurutani et al., 2016a,b; Hajra and Tsurutani, 2018; Hajra, 2021b), auroral ionosphere (Tsurutani and Gonzalez, 1987; Hajra et al., 2013, 2017; Kilpua et al., 2013; Kilpua et al., 2017) and atmosphere (Lei et al., 2011; Gardner et al., 2012). While there are apparent similarities between the two types of space weather events, there are significant differences in their solar sources, solar-cycle variations, and impacts.

As mentioned above, sheaths are associated with CMEs erupted from the active regions on the Sun, while CIRs are associated with HSSs emanated from the solar coronal holes. This leads to their varying solar-cycle variations. In addition, a major fraction of the strongest storms is known to be caused by the sheaths (Tsurutani et al., 1988; Huttunen et al., 2002; Huttunen and Koskinen, 2004; Echer et al., 2008), while CIRs are known to be responsible for a major fraction of the moderate storms at the Earth (Alves et al., 2006; Chi et al., 2018; Hajra and Sunny, 2022).

While the CIR and sheath characteristics and their impacts on Earth are well explored topics, further statistical studies are required for a deeper understanding of the events, and their impacts. Here we will present a compact study on both the characteristics and impacts of CIRs and sheaths and a comparison between CIRs and sheaths with respect to their characteristics, geoeffectiveness and solar cycle variations. The aim of this present work is to conduct a detailed comparison of their solar-cycle variations, solar-wind and IMF characteristic features, and impacts on the magnetosphere-ionosphere system. The aim of the present work is to develop an updated catalogue of all CIRs and sheaths encountered by Earth during the most recently completed solar cycle 24, from January 2008 through December 2019. The catalogue can be utilized by the space weather research community for various research, modelling and space mission planning.

Using all available solar wind plasma and magnetic field measurements upstream of the Earth, the general plasma and magnetic field characteristic features of the CIRs and sheaths will be identified. These can be used as the typical features of these events for modelling purpose. It can be noted that most of the previous works used the spacecraft in situ solar wind measurements, which are far from the Earth. In contrast, we will use the solar wind plasma and magnetic field measurements shifted to the Earth’s bow shock nose considering the solar wind propagation time from the spacecraft to the bow shock. These shifted data are more suitable to study the near-Earth CIR and sheath characteristics, and for a direct comparison with the magnetospheric response. The geoeffectiveness of the CIRs and sheaths in causing geomagnetic storms will be studied using geomagnetic measurements. The relationships of the CIR and sheath characteristics with geomagnetic indices will also be explored. This study will hopefully enhance the prediction capacity of CIRs and sheaths and the geomagnetic activity related to these two events.

1.6. Organization of Thesis

This Thesis work contains the study of corotating interaction regions and interplanetary sheaths during solar cycle 24. Even though both CIRs and sheaths are having common solar origin both are distinct in many aspects. This work contains a statistical study of their seasonal dependance, potential in creating geoeffectiveness and characteristics of its various parameters.

Chapter 2 provides the sources of all the data used in this work, and describes various methods used to analyze the data.

Chapter 3 describes the main results obtained in this work. The results are discussed in the context of past works in this field in order to highlight new findings of the present work.

Chapter 4 lists the major conclusions from the present work and scope of future work.

Chapter 2

Database and Methods

2.1. Data Sources

Solar Wind Plasma

CIRs and Sheaths are identified using high-resolution (one-minute) solar-wind plasma and interplanetary magnetic-field (IMF) data collected from NASA's OMNI Web (https://omniweb.gsfc.nasa.gov/). These are observations made by the ACE, Wind, IMP 8, and Geotail spacecraft upstream of the Earth, which are shifted in time to take into account the arrival time of the solar wind to the Earth's bow-shock nose. The time-shifting is important for a direct comparison of the solar-wind variations with their geomagnetic impacts. In addition, the multi-spacecraft-based OMNI database can give complete and reliable statistics of CIRs encountered by Earth than any single spacecraft observation reported previously.

IMF Measurements

The IMF measurements are in the geocentric solar magnetospheric (GSM) coordinate system, where the x-axis is directed towards the Sun and the y-axis is in the $\boldsymbol{\Omega} \times \hat{\boldsymbol{x}}/|\boldsymbol{\Omega} \times \hat{\boldsymbol{x}}|$ direction, $\boldsymbol{\Omega}$ is aligned with the magnetic south pole axis of the Earth. The z-axis completes a right-hand system.

SDO Observatory

Solar sources of the streams are identified by exploring the solar coronal images (at wavelength of 193 Å) taken by the Atmospheric Imaging Assembly (AIA) telescope of NASA's Solar Dynamics Observatory (SDO; https://sdo.gsfc.nasa.gov/). NASA's Solar Dynamics Observatory or SDO is a geosynchronous satellite which helps us in explaining the source of Sun's energy, how the inside Sun works and how its atmosphere stores and releases energy in dramatic eruptions. Since its launch in 2010 SDO has studied about how the Sun creates solar activity and how it drives the space weather i.e., the dynamic conditions in space that can cause impacts in the entire solar system, including Earth.

SDO in every twelve seconds captures the images of Sun in ten wavelengths of Ultraviolet light.

CME Catalogue

To verify solar sources of sheaths we explored the CME catalogue available at the Coordinated Data Analysis Workshops (https://cdaw.gsfc.nasa.gov/). The CDAW catalog contains all CMEs which are identified manually since 1996 from the Large Angle and Spectrometric Coronagraph (LASCO) on board the Solar and Heliospheric Observatory (SOHO) mission.

Geomagnetic Indices

The SYM-H and AE indices (1 minute) are obtained from the World Data Center for Geomagnetism, Kyoto, Japan (http://wdc.kugi.kyoto-u.ac.jp/). SYM-H indicates the intensity of a magnetic storm. It is similar to the Dst (1 hr) index but have a much higher time-resolution (1 minute). SYM-H index is used to identify storms which occur when the value of SYM-H goes less than -50nT. This index is used in describing the geomagnetic disturbances at mid-latitudes in terms of longitudinally symmetric (SYM) disturbances for H perpendicular to the dipole axis. It measures the variations of the horizontal component of the Earth's magnetic field due to the ring current and therefore the strength of a magnetic storm.

The Auroral Electrojet (AE) index describes the disturbance level recorded by the auroral zone magnetometers. The AE index is related to the auroral ionospheric currents at ~ 100 km altitude. The set of globe encircling stations records the horizontal magnetic components, these data are plotted to the same time and amplitude scale relative to their quiet-time levels and are then graphically superposed. Amplitude Upper (AU) defines the upper envelopes and Amplitude Lower (AL) represents the lower envelop of the superposition respectively. Thus, AE is defined as the difference between AU and AL i.e., AE = AU – AL.

$F_{10.7}$ Solar Flux

Phases of the ≈ 11-year solar cycle (Schwabe, 1844) are identified using the daily $F_{10.7}$ solar flux obtained from the Laboratory for Atmospheric and Space Physics (LASP)

Interactive Solar Irradiance Data Center (https://lasp.colorado.edu/lisird/). The $F_{10.7}$ index measures the noise level generated by the Sun at a wavelength of 10.7 cm at the earth's orbit. The solar radio flux at 10.7 cm (2800 MHz) can be used as an excellent indicator of solar activity. The $F_{10.7}$ radio emissions originate high in the chromosphere and low in the corona of the solar atmosphere. The $F_{10.7}$ correlates well with the number of sunspots and with the number of ultra violet (UV) and visible solar irradiance records. AS EUV cannot be measured from ground due to atmospheric absorption, the solar flux density at a wavelength of 10.7 cm has been used as a proxy since 1947. The 10.7 cm solar flux measurement denotes the strength of solar radio emission in a 100 MHz wide band centered on 2800 MHz, averaged over an hour. It is expressed in solar flux units (sfu), where 1 sfu = 10^{-22} Wm^{-2} Hz^{-1}

2.2. Methods

CIR Identification

CIRs are identified manually as follows. First, from the temporal variation of the solar wind plasma speed V_{sw}, streams with $V_{sw} > 500$ km s^{-1} are identified as "potential" HSSs. Second, the solar sources of the streams are identified by exploring the solar coronal images (at wavelength of 193 Å) taken by the Atmospheric Imaging Assembly (AIA) telescope of NASA's Solar Dynamics Observatory (SDO; https://sdo.gsfc.nasa.gov/). Properties of the coronal holes, like location on the Sun, magnetic polarity, were determined from the solar synoptic maps available at the Space Weather Prediction Center of National Oceanic and Atmospheric Administration (NOAA; https://www.swpc.noaa.gov/). The streams, depending on their speed between ≈ 500 and 800 km s^{-1}, can travel from the Sun to 1 AU in ≈ 2.0-3.5 days. If a coronal hole is identified (in the SDO/AIA images) within ≈ 2-3 days preceding the potential HSS identification at 1 AU, the stream is confirmed as a coronal hole emanated HSS. Third, for the confirmed HSS cases, the solar wind plasma with enhanced density N_{sw}, ram pressure P_{sw} and IMF magnitude B_0 in the interaction region between a slow stream and a HSS is identified as a CIR event.

Sheath Identification

Sheaths are identified from the temporal variation of solar-wind parameters as follows. First, interplanetary fast forward shocks are identified by the abrupt increases in the solar-wind speed V_{sw} with simultaneous increases in plasma density N_{sw}, temperature T_{sw}, and B_0. Second, to confirm the CME eruption as the solar source of the identified shocks, CDAW CME catalogue was explored (https://cdaw.gsfc.nasa.gov/). Third, prominent ICME MC signatures are verified by low T_{sw}, plasma β and/or smooth rotation(s) in the IMF component(s). Finally, the compressed plasma and magnetic field region between a fast forward shock and an ICME is identified as a sheath.

Geoeffectiveness

In this work, a CIR is defined to be geoeffective if it causes a geomagnetic storm with the SYM-H peak (minimum) ≤ −50 nT (Gonzalez et al., 1994). During a geomagnetic storm, the westward ring current, encircling the Earth's magnetic equator at an altitude of ≈ 2-7 Earth radii ($R_\oplus$), is enhanced due to injection of energetic (≈ 10-300 keV) particles (e.g., H^+, He^{2+}) from the solar wind and acceleration of the terrestrial thermal ions (O^+) (Frank, 1967; Shelley et al., 1972; Williams, 1987; Hamilton et al., 1988; Daglis et al., 1999). As a consequence, the low-latitude geomagnetic fields decrease, which is measured by the SYM-H index (Wanliss and Showalter, 2006; Iyemori et al., 2010). Following Gonzalez et al. (1994), storms are classified as moderate (−50 nT ≥ SYM-H > −100 nT) and intense (SYM-H ≤ −100 nT) storms. We also studied the CIR impacts on the auroral ionosphere using the auroral electrojet (AE) index (Davis and Sugiura, 1966). The SYM-H and AE indices (1 minute) are obtained from the World Data Center for Geomagnetism, Kyoto, Japan (http://wdc.kugi.kyoto-u.ac.jp/). Phases of the ≈ 11-year solar cycle (Schwabe, 1844) are identified using the daily $F_{10.7}$ solar flux obtained from the Laboratory for Atmospheric and Space Physics (LASP) Interactive Solar Irradiance Data Center (https://lasp.colorado.edu/lisird/).

Wavelet Analysis

With the non-stationary variations in interplanetary and magnetospheric parameters the interplanetary and magnetospheric environments became complex and turbulent (Souza et al., 2016; Marques de Souza et al., 2018). The temporal variability of the power spectral density in such media is studied by using the Wavelet Transforms (WT).The mother function shown in Equation 1 generates the wavelet function $\psi(t)$. The mother function suffers an expansion: $\psi(t) \rightarrow \psi(2t)$, and a translation: $\psi(t) \rightarrow \psi(t + 1)$ in time, resulting in wavelet-daughter functions (Torrence & Compo, 1998):

$$\psi_{a,b}(t) = \frac{1}{\sqrt{a}} \psi\left(\frac{t-b}{a}\right), \text{ for } a,b \in Z \text{ and } a \neq 0 \tag{1}$$

In equation 1, a is the scale associated to wavelet expansion and contraction, and b is the temporal location, related to translation in time. The Wavelet Transform applied on f(t) time series is:

$$WT(a,b) = \int f(t)\, \psi^{*}_{a,b}(t)\, dt \tag{2}$$

Where $\psi^{*}_{a,b}(t)$ represents the complex conjugate of the wavelet function $\psi_{a,b}(t)$.

Cross Correlation Analysis

We use the classical cross correlation analysis to study the yearly occurrences of sheaths and CIRs with yearly mean $F_{10.7}$ solar flux (Davis, 2002). The cross-correlation between two time series is computed by displacing one time series relative to the other in time (t) units. From this the correlation coefficients, successive lags, and the lag corresponding to the maximum correlation between two time series can be obtained. In cross correlation a zero lag corresponds linear correlation where the time series are aligned. The cross-correlation coefficient (r) between time series Y_1 and Y_2 with n overlapped positions is defined as:

$$r = \frac{n\Sigma Y_1 Y_2 - \Sigma Y_1 \Sigma Y_2}{\sqrt{\left[n\Sigma Y_1^2 - (\Sigma Y_1)^2\right]\left[n\,\Sigma Y_2^2 - (\Sigma Y_2)^2\right]}} \tag{3}$$

This varies from -1 to +1 and tells how the two series are correlated. When $r = 0$, then no correlation exists between the two-time series. The correlation is positive for $r > 0$, which is the maximum for $r = 1$. When $r < 0$ it means anti correlation, with $r = -1$ corresponds a perfect anti-correlation.

Variance Analysis

Variance analysis is used to study the variance of IMF components of sheaths and CIRs. The variance is the measure of variability which is calculated by taking the average of squared deviations from the mean. The variance is calculated using the following equation:

$$\sigma^2 = \frac{\Sigma\,(X - \mu)2}{N} \tag{4}$$

Where σ is the standard deviation, X is individual value μ is population mean and N is number of events.

Lomb-Scargle periodograms

The Lomb-Scargle periodogram (Lomb 1976; Scargle 1982) is a statistical tool which is used commonly to detect the periodic signals in unevenly spaced observations. The Lomb-Scargle periodogram allows us to compute efficiently a Fourier-like power spectrum from unevenly sampled data, which results in an initiative means of determining the periods of oscillation (see VanderPlas, 2018). In this work Lomb-scargle is preferred over Fourier Transform as the latter will not work for unevenly spaced data.

Wilcoxon Rank Sum Test

We used Wilcoxon Rank Sum test to study the samples of sheaths and CIRs. Wilcoxon Rank Sum test is a non-parametric test for two samples which is described by Wilcoxon and studied by Mann and Whitney. This test is used widely as an alternative to the t-test when our sample is not normally distributed (for references see Nonparametric Statistical Inference by J. D. Gibbons & S. Chakraborti).

Chapter 3

Results and Discussions

3.1. Case studies of CIRs and Sheaths: interplanetary characteristics and geoeffectiveness

Figure 3.1 shows solar-wind variations and geomagnetic impacts of a CIR occurring during days 68 – 69 of year 2008, and an interplanetary sheath during days 215 – 216 of year 2010. Top panels, from Figure 3.1a to Figure 3.1l, depict the solar-wind and interplanetary conditions. Bottom panels, from Figure 3.1m to Figure 3.1p, show the geomagnetic conditions.

The CIR (Figure 3.1, left panel) is formed between a slow solar wind with V_{sw} of ≈ 325 km s^{-1} on days 67 – 68 and an HSS with a peak V_{sw} of ≈ 738 km s^{-1} on day 71 of year 2008. The solar source of the HSS is a large, positive polarity coronal hole (marked by number 50), prominently visible from the equator to the south hemisphere of the Sun on days 68 – 69 (not shown). Figure 3.2a shows the solar source of HSS from the sun which is collected from SDO observatory of NASA (https://www.spaceweather.com/). The CIR interval extended from ≈ 0656 UT on day 68 to ≈ 1254 UT on day 69 (marked by a blue shading in Figure 3.1, left panel). While there is no sharp boundary of the CIR (in the solar-wind data), it is identified by gradually increasing B_0 peaking to ≈ 18 nT at 0521 UT on day 69, followed by its gradual decrease. While the IMF components are highly fluctuating during the HSS proper, the fluctuation amplitude is significantly enhanced during the CIR interval. N_{sw} and P_{sw} are also compressed, with peak values of ≈ 41 cm^{-3} and ≈ 13 nPa, respectively during the CIR event.

Magnetospheric compression by the P_{sw} enhancement at the CIR leading edge is associated with a gradual increase in SYM-H to 32 nT (Figure 1o). This was followed by two episodes of southward IMF with the minimum B_z of ≈ −15 nT and ≈ −13 nT and duration of ≈ 1.78 hours and ≈ 1.77 hours, respectively. These are correlated with AE increases with the maximum AE values of 941 nT and 737 nT, and the minimum SYM-H values of −17 nT and −38 nT, respectively. A stronger (B_z minimum ≈ −16 nT) and longer-duration (≈ 2.48 hours) IMF southward component led to a stronger SYM-H negative excursion to −100 nT at ≈ 0540 UT on day 69. This was associated with an AE increase to 1341 nT. Thus, the CIR is found to be geoeffective causing an intense magnetic storm with a three-step main phase development.

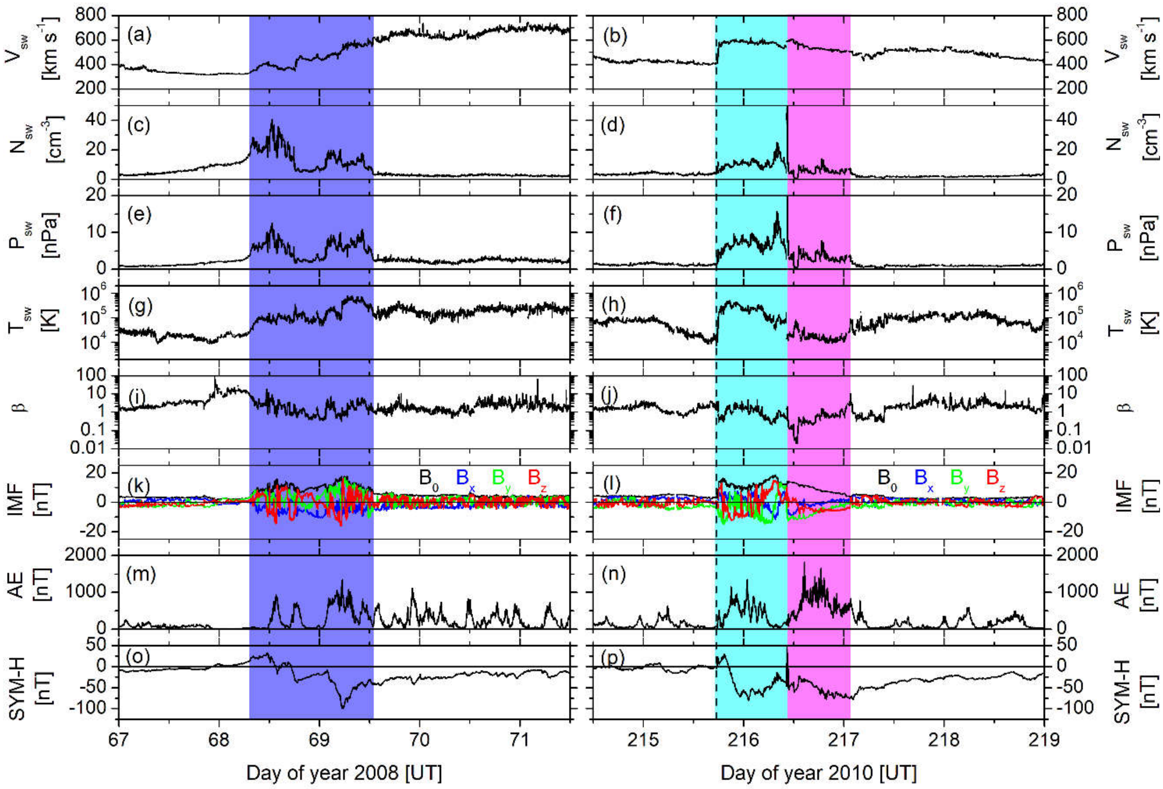

Figure 3.1. Solar-wind variations and geomagnetic effects during days 67 – 71 of year 2008 (left) and days 214 – 218 of year 2010 (right). From top to bottom, the panels show (a – b) solar-wind plasma speed [V_{sw}], (c – d) plasma density [N_{sw}], (e – f) ram pressure [P_{sw}], (g – h) temperature [T_{sw}], (i – j) plasma-β, (k – l) IMF magnitude [B_0], and B_x-, B_y-, B_z- components, and geomagnetic indices (m – n) AE, and (o – p) SYM-H. The shaded regions show a CIR (blue), a sheath (light cyan) and an MC (light magenta). The vertical dashed line in the right panel shows an interplanetary fast forward shock.

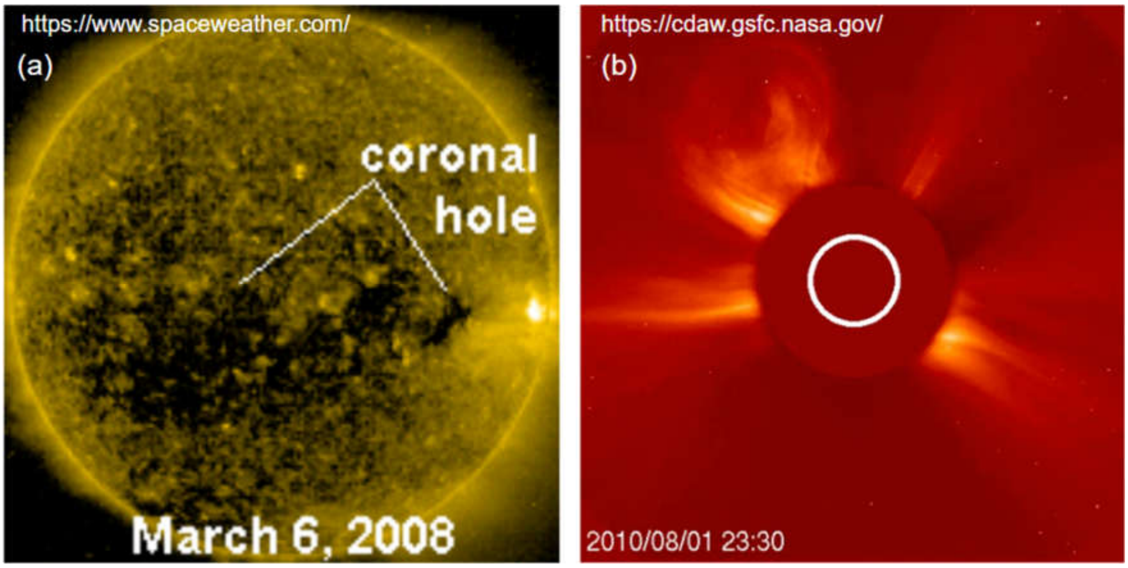

Figure 3.2. Solar sources (a) Solar image taken by the SDO/AIA telescope at the wavelength of 193 Å. The dark regions around the centre show the coronal holes. The coronal holes on 6 March (day 66) 2008 is the sources of HSSs identified on days 69. (b) CME eruption image taken by SOHO observatory. The CME is recorded on 1 August (day 213) 2010 which reaches the earth surface on day 215.

The interplanetary structures during days 214 – 217 of year 2010 (Figure 3.1, right panel) are associated with a halo CME that was erupted at a speed of 850 km s^{-1} from the Sun at ≈ 1342 UT on day 213 (shown in figure 3.2b). The interplanetary counterpart of the CME (i.e., ICME), moving faster than the ambient solar wind, caused a fast FS at ≈ 1743 UT on day 215 (marked by a vertical dashed line). The FS can be identified by sharp and simultaneous increases in V_{sw} from ≈ 409 to 585 km s^{-1}, in N_{sw} from ≈ 3.6 to 11.9 cm^{-3}, in P_{sw} from ≈ 1.5 to 5.4 nPa, in T_{sw} from ≈ 1.0×10^4 to 1.6×10^5 K, and in IMF B0 from ≈ 3.3 to 14.0 nT. This caused a sudden impulse (SI^+) of +23 nT in SYM-H (Figure 3.1p).

The FS is followed by a sheath up to ≈ 1038 UT on day 216. This is characterized by strong fluctuations in the IMF components, and enhancements in B_0 (≈ 18.7 nT), V_{sw} (≈ 604 km s^{-1}), N_{sw} (≈ 24.9 cm^{-3}), P_{sw} (≈ 15.7 nPa), and T_{sw} (≈ 5×10^5 K). IMF B_z shows long-duration southward component with peak of −12.6 nT. This led to a moderate magnetic storm with the SYM-H minimum of −81 nT at ≈ 0110 UT on day 216.

Following the sheath, the IMF components show smooth rotations up to ≈ 0122 UT on day 217. This interval is characterized by a minimum T_{sw} of ≈ 1.0×10^4 K and a minimum β of 0.02. This represents a flux-rope magnetic cloud (MC: Burlaga et al., 1981; Klein and Burlaga, 1982; Tsurutani and Gonzalez, 1997). However, a detailed study of the MC is beyond the scope of the present work.

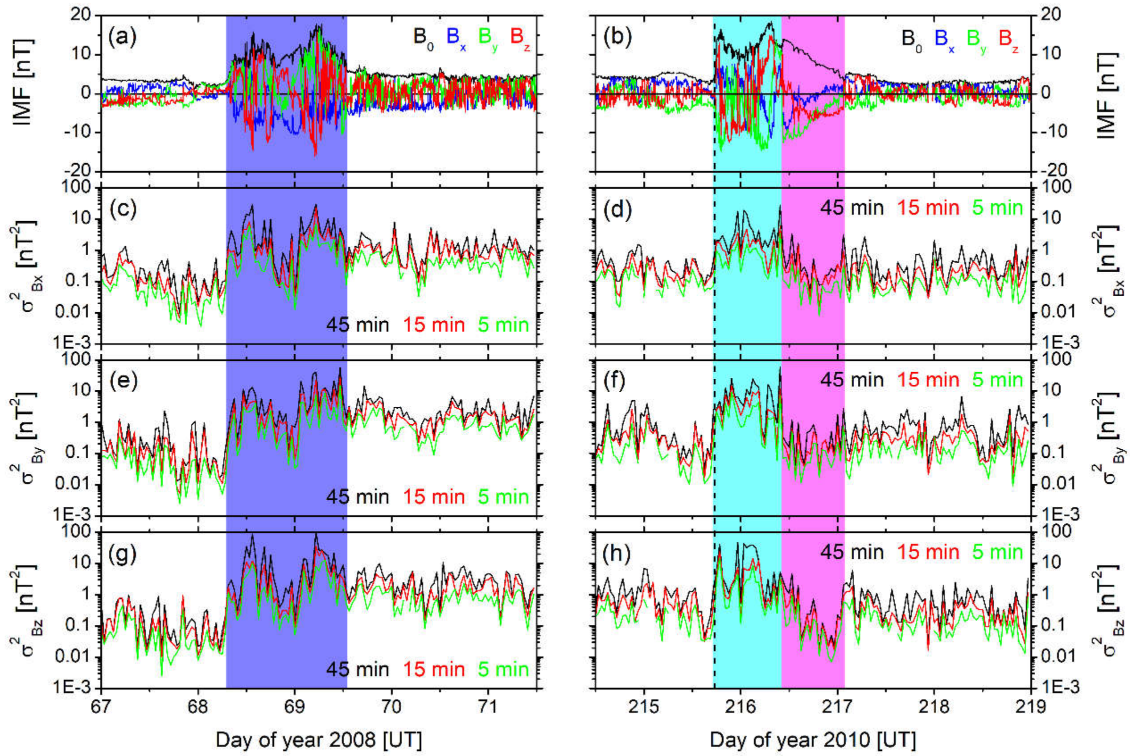

Figure 3.3. Variations of IMF during days 67 – 71 of year 2008 (left) and days 214 – 218 of year 2010 (right). From top to bottom, panels are (a – b) IMF B_0 (black) and B_x- (blue), B_y- (green), and B_z- (red) components, variances in (c – d) B_x, (e – f) B_y, and (g – h) B_z. Markings of interplanetary structures are repeated from Figure 3.1 for a reference.

Most prominent and common feature of the sheath and CIR shown in Figure 3.1 is fluctuations in the IMF components. Kilpua et al. (2013) investigated ultra-low frequency (ULF) IMF and P_{sw} fluctuations (corresponding period of 3 – 10 minutes) for 41 sheaths during Solar Cycle 23. Moissard, Fontaine, and Savoini (2019) identified high levels of turbulent energy in the IMF fluctuations during 42 sheaths between 1998 and 2006.

To study the IMF fluctuations during the CIR and the sheath, we estimated the IMF-component variances (Figure 3.3) during the events shown in Figure 3.1. With the commencement of the CIR (Figure 3.3, left panel), variances increase in all IMF-components compared to their values before the CIR impact. While IMF B_0 is significantly high during the CIR compared to that during the following HSS interval, variances during the HSS interval are comparable to those during the CIR. High IMF variances during the CIR/HSS are associated with Alfven wave activity.

The IMF variances during the sheath (Figure 3.3, right panel) are almost identical to those during the CIR. The variances clearly increase during the sheath than those before the shock commencement. Interestingly, variances decrease during the MC that is characterized by smooth rotations in the IMF components.

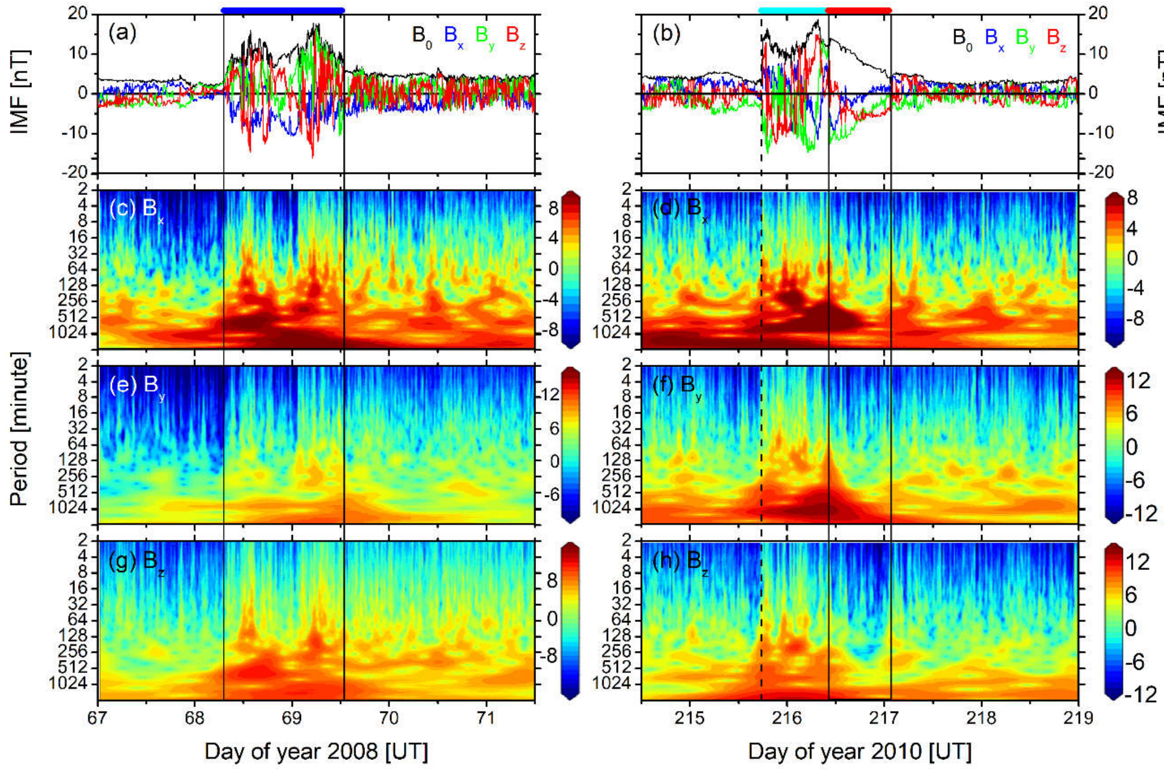

Figure 3.4. Wavelet analysis of IMF during days 67 – 71 of year 2008 (left) and days 214 – 218 of year 2010 (right). From top to bottom, panels are (a – b) IMF B_0 (black) and B_x- (blue), B_y- (green), and B_z- (red) components, wavelet spectrum of (c – d) B_x, (e – f) B_y, and (g – h) B_z. The color bars on the right of each wavelet spectrum indicate the wavelet spectral power of the observed periods in arbitrary units. Horizontal bars at the top indicate a CIR (blue), a sheath (cyan), and an MC (red). An interplanetary shock is shown by a vertical dashed line.

Figure 3.4 shows the continuous Morlet wavelets of the IMF components. Compared to the pre-CIR interval (Figure 3.4, left panel), smaller-period (that is, higher-frequency) fluctuations are found to enhance in amplitude during the CIR and HSS intervals. This is most prominent in the B_z-component (Figure 3.4g), where strong power can be noted from ≈ 15 minutes to a few hours. Enhanced power of the lower-period fluctuations during the sheath is followed by disappearance of the same during the following MC interval (Figure 3.4, right panel).

The above results are further confirmed by Lomb-Scargle periodogram analysis shown in Figure 3.5. For this, 4-hour intervals are selected before the CIR (marked as low-speed stream or LSS), during the CIR, during the HSS, before the sheath impact, during the sheath, and during the MC. These are marked by color-coded bars at the top of Figure 3.5. Both during the CIR (Figure 3.5e) and the sheath (Figure 3.5f), 30 minutes- to 1 hour- periods have statistically significant (above the 95 % confidence level) power. This result again confirms high-frequency fluctuations or turbulent nature of CIR and sheath.

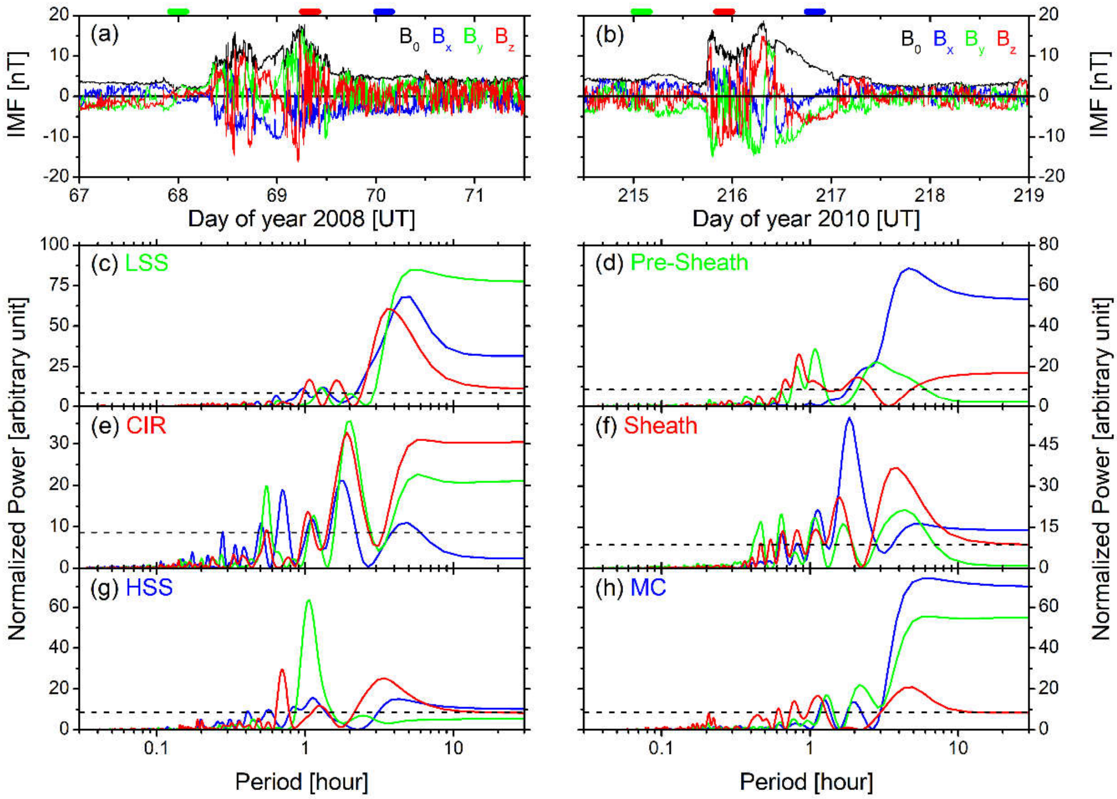

Figure 3.5. Lomb-Scargle periodograms of IMF during days 67 – 71 of year 2008 (left) and days 214 – 218 of year 2010 (right). From top to bottom, panels are (a – b) IMF B_0 (black) and B_x- (blue), B_y- (green), and B_z- (red) components, periodograms during (c) low-speed stream (LSS), (d) interval before sheath, (e) CIR, (f) sheath, (g) HSS, and (h) MC. Durations of the periodograms are shown by color-coded bars at the top panel. The 95 % confidence level of the periodograms is shown by the horizontal dashed lines.

3.2. Solar cycle and seasonal variations of CIRs and sheaths

Following the method described in Chapter 2, we identified a total of 290 CIRs from January 2008 to December 2019. The CIR events are shown as a year-month contour plot in Figure 3.6b. The superposed numbers of events in each year and each month are shown as histograms in Figures 3.6a and 3.6c, respectively, along with the associated Poisson counting error bars. Most prominent features noted from Figure 3.6b are the largest population of events during the years 2015-2017 (yearly 34, 35 and 31 events, respectively), and the smallest occurrence during 2014 (only 11 events). From the variation of the yearly mean $F_{10.7}$ solar flux (Figure 3.6a, red), the year 2014 corresponds to the maximum of the solar cycle 24, while the years 2015-2017 are in the descending phase. The solar flux is expressed in the solar flux unit (sfu) where 1 sfu = 10^{-22} W m^{-2} Hz^{-1}.

Based on the $F_{10.7}$ solar flux values, the entire period of study (from January 2008 to December 2019) is divided into: the solar minimum (years 2008-2009 and 2018-2019 with $F_{10.7}$ of ≈ 69-71 sfu), the ascending phase (years 2010-2013 with $F_{10.7}$ of ≈ 80-123 sfu), the maximum (year 2014 with $F_{10.7}$ of ≈ 146 sfu), and the descending phase (years 2015-2017 with $F_{10.7}$ of ≈ 77-118 sfu), as shown by the horizontal colour coded bars in Figure 3.6a (top). The CIR occurrence rate is found to be the highest during the descending phase (≈ 33 year^{-1}), followed by occurrences during the solar minimum (≈ 24 year^{-1}), the ascending phase (≈ 22 year^{-1}), and the solar maximum (≈ 11 year^{-1}). It can be mentioned that Alves et al. (2006) studied all near-Earth CIRs during 1964-2003, without exploring such solar cycle dependence. Jian et al. (2006) studied the near-Earth CIRs encountered by the Wind and ACE spacecraft during 1995-2004, and reported only little variation in their annual numbers. Jian et al. (2019) surveyed all CIRs encountered by the *Solar Terrestrial Relations Observatory* (STEREO) spacecraft during 2007-2016 indicating larger number of events during the descending phase. However, no such quantitative result of the solar cycle phase dependence (as reported in the present work) was reported.

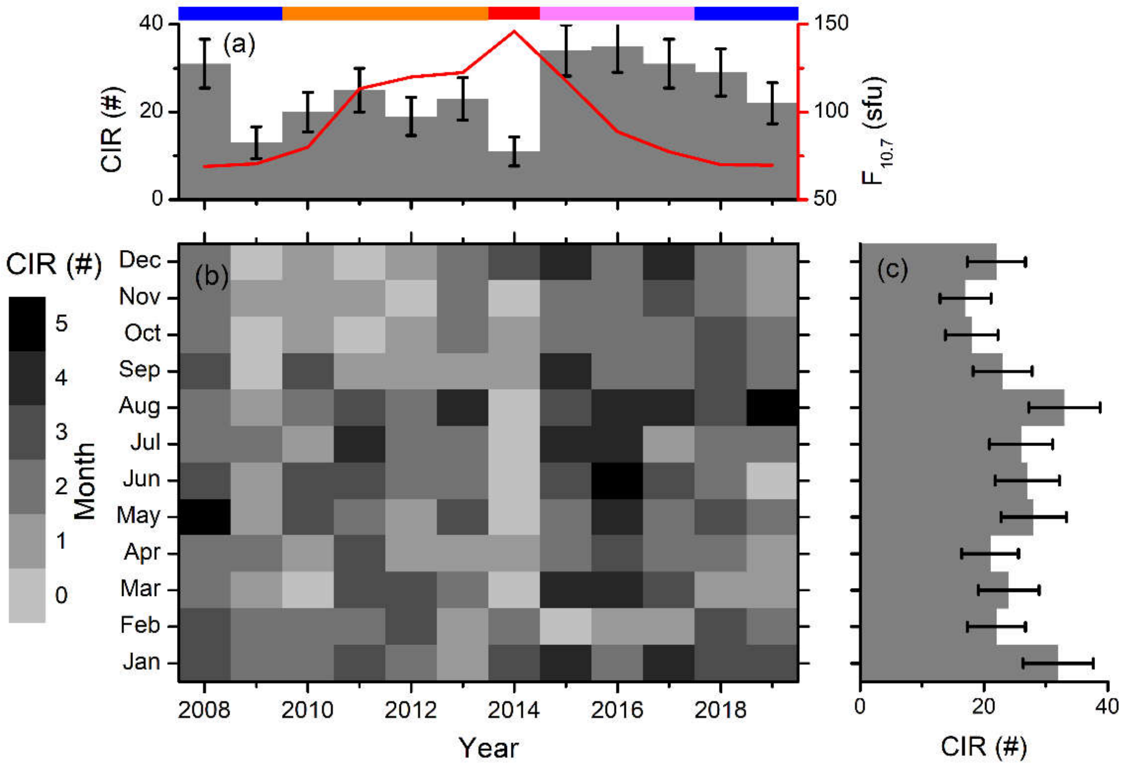

Figure 3.6. Seasonal and solar cycle dependence of CIRs. (a) Yearly number of CIRs (histograms, legend on the left) with Poisson counting errors (vertical bars), and yearly mean $F_{10.7}$ solar flux (red, legend on the right), (b) year-month contour plot of CIRs, values of different shading are given in legend on the left, (c) monthly number of CIRs with Poisson counting error bars. The solar cycle phases are shown by colour coded horizontal bars at the top, as the solar minimum (blue), the ascending phases (orange), the maximum (red), and the descending phase (pink).

The above-mentioned solar cycle dependence of the CIRs can be explained as a result of varying coronal hole size and location with the ≈ 11-year solar cycle. The coronal holes are normally located near the polar regions of the Sun at the solar maximum. However, the holes expand in size and move towards equator during the solar cycle descending phase and the solar minimum (Burlaga et al., 1978; Sheeley and Harvey, 1981). HSSs emanated from the equatorial coronal holes and the consequent CIRs have higher probability of encountering with Earth in the ecliptic plane of the Sun.

Thus, the near-Earth CIR occurrence rate is higher during the descending to minimum solar cycle phases compared to the solar maximum and ascending phases (Richardson et al., 2000; Tsurutani et al., 2006).

As expected, the CIR distribution does not exhibit any seasonal dependence (Figure 3.6c). During the entire period of observation, the largest number of events (33) are recorded during August with a comparable number (32) during January, and the smallest number (17) during November.

For the case of interplanetary sheaths, as per the method discussed in Chapter 2 for the identification of sheaths, a total of 110 sheaths were identified from January 2008 to December 2019. The sheath events are shown as a year-month contour plot in Figure 3.7b. The superposed numbers of events in each year and each month are shown as histograms in Figures 3.7a and 3.7c, respectively, along with the associated Poisson counting error bars. The largest population of events were recorded during the years 2010-2013 with 7, 14, 21 and 14 events per year respectively and smallest were occurred during year 2008-2009 and 2018-2019 with 3, 10, 4, 4 events. From the yearly mean $F_{10.7}$ solar flux variation, the years 2010-2013 corresponds to the ascending phase of Solar cycle 24 and years 2008-2009 and 2018-2019 are in the minimum phase. The solar flux is expressed in the solar flux unit (sfu) where 1 sfu = 10^{-22} W m^{-2} Hz^{-1}.

As shown by the horizontal colour coded bars in Figure 3.7a (top). As per the yearly mean $F_{10.7}$ solar flux the sheath occurrence rate is found to be the highest during the ascending phase (≈ 14 $year^{-1}$), followed by occurrences during the solar maximum (≈ 11 $year^{-1}$), the descending phase (≈ 7 $year^{-1}$), and the solar minimum (≈ 5 $year^{-1}$). But comparing with the monthly $F_{10.7}$ Solar flux (shown in Figure 3.7a in blue) the highest number of sheaths corresponds to the maximum phase of solar cycle. Since the Solar Cycle 24 was peculiar with two maximums one in 2012 and other in 2014.

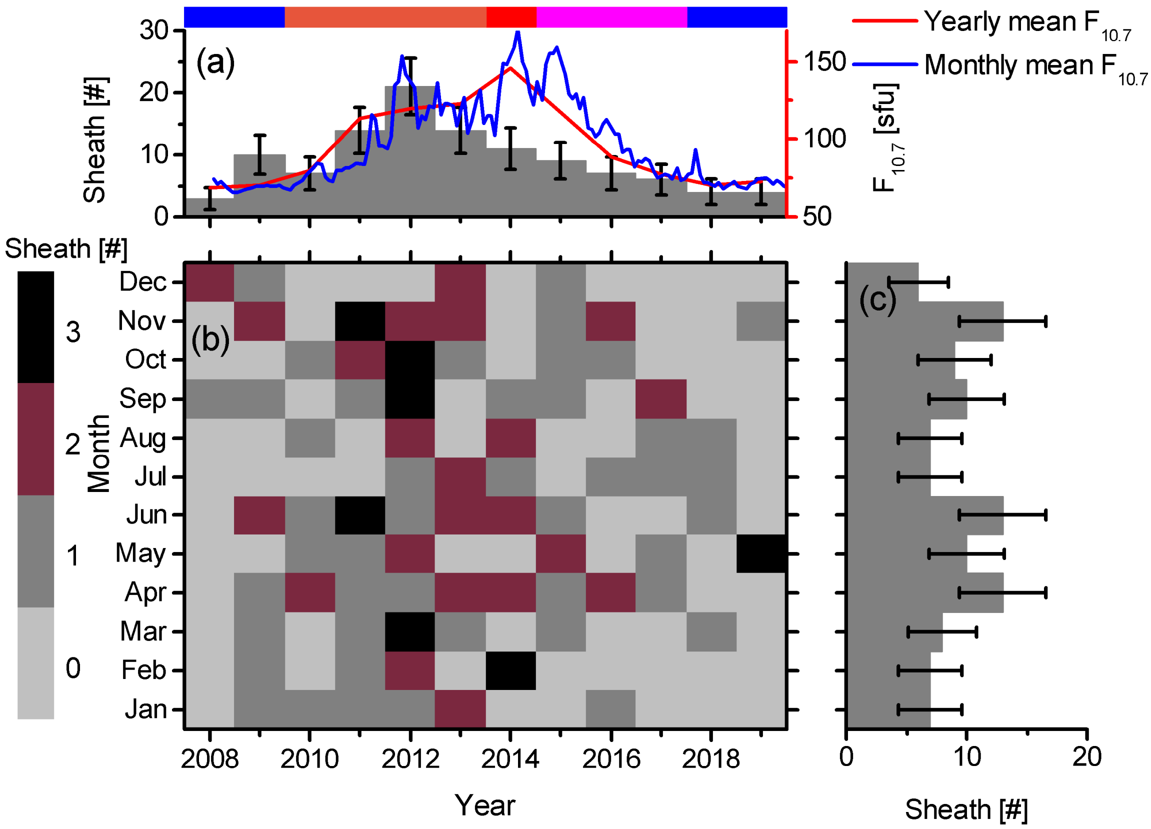

Figure 3.7. Seasonal and solar cycle dependence of sheaths. (a) Yearly number of sheaths (histograms, legend on the left) with Poisson counting errors (vertical bars), yearly mean $F_{10.7}$ solar flux (red, legend on the right) and monthly mean $F_{10.7}$ solar flux (blue, legend on the right), (b) year-month contour plot of sheaths, values of different shading are given in legend on the left, (c) monthly number of sheaths with Poisson counting error bars. The solar cycle phases are shown by colour coded horizontal bars at the top, as the solar minimum (blue), the ascending phases (orange), the maximum (red), and the descending phase (pink).

The solar cycle dependence of the sheaths mentioned above can be describes as, since number of ICME occurrence is maximum during the solar maximum period (e.g., Webb and Howard, 1994; Gopalswamy et al., 2004; Tsurutani et al., 2006; Obridko et al., 2012), the number of sheath occurrence will also be highest during this period. The highest number of sheaths (22) were recorded in 2012, this can be attributed to the fact that Solar Cycle 24 was having two peaks one during November 2011, and another during February 2014 (shown in Figure 3.7a in blue).

The sheath distribution also does not exhibit any seasonal dependence (Figure 3.7c). During the entire period of observation, the largest number of events (13) are recorded during April (spring), June (summer) and November (winter) and the smallest number (6) during December with a comparable number (7) in January and February.

On comparing solar cycle dependence of sheaths and CIRs, Figure 3.8a shows the solar cycle variations of all sheaths (110) and CIRs (290) under this study. The yearly occurrences are computed from the total number of the events in each year as percentage of total number during the entire period of observation. As shown by the yearly mean $F_{10.7}$ solar flux variation, solar activity is significantly high during the years 2012 to 2015, with the maximum yearly mean flux in 2014. The sheath occurrence follows the $F_{10.7}$ variation, attaining a peak in 2012. It can be noted that, when considering the monthly mean $F_{10.7}$ solar flux, Solar Cycle 24 has two peaks: one peak during November 2011, and another during February 2014 (shown in Figure 3.7a in blue). Thus the 2012 sheath peak seems to be associated with the first solar activity peak. The association of the sheath occurrence with the $F_{10.7}$ variation is confirmed by a high cross-correlation coefficient (rcc) of +0.71 at 0-year time lag between the two (Figure 3.8b). The sheath solar cycle variation is found to be consistent with the solar cycle variation of the driving ICMEs (see Richardson and Cane, 2012; Wu and Lepping, 2016; Kilpua et al., 2017, and references therein).

On the other hand, the CIR occurrence is much more uniformly distributed through the solar cycle, with slightly higher occurrence during the descending to minimum phases of the solar cycle (Figure 3.8a). This solar cycle variation pattern is reflected in comparatively lower cross-correlation coefficient of the CIR occurrence at −2-year (rcc = −0.53) and +4-year (rcc = +0.50) time lags with the $F_{10.7}$ solar flux. The CIR solar cycle variation is consistent with previous works (e.g., Alves et al., 2006; Jian et al., 2006, 2019; Hajra and Sunny, 2022).

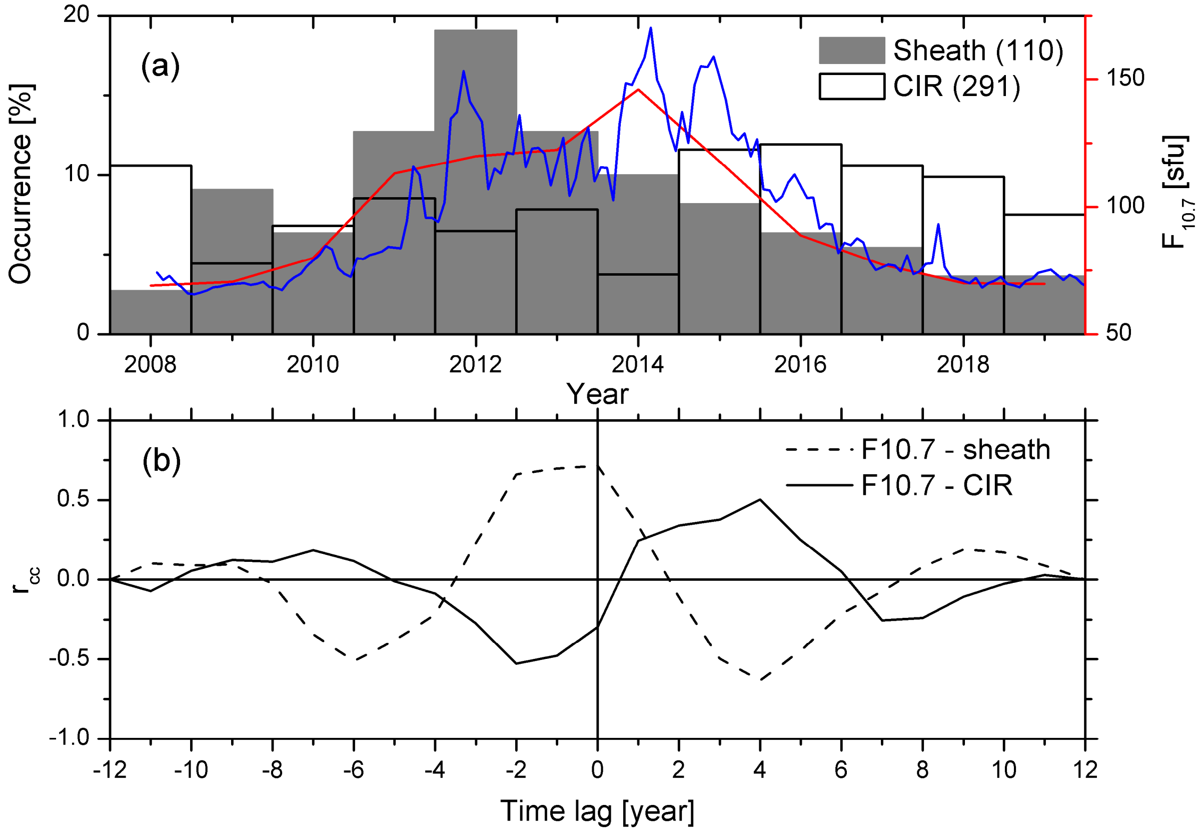

Figure 3.8. (a) Yearly occurrences (scale on the left) of sheaths (gray histogram) and CIRs (Empty histogram), yearly mean $F_{10.7}$ solar flux (red, scale on the right) and monthly mean $F_{10.7}$ solar flux (blue, scale on the right). (b) Cross correlations (rcc) of yearly occurrences of sheaths and CIRs with yearly mean $F_{10.7}$ solar flux. The $F_{10.7}$ is given in solar flux unit (sfu), where 1 sfu = 10^{-22} Wm^{-2} Hz^{-1}.

3.3. Geoeffectiveness of CIRs and sheaths

Among all of the 290 CIR events identified in this work, only 88 (i.e., ≈ 30 % of the CIRs) caused geomagnetic storms with the SYM-H peak ≤ −50 nT (Table 3.1). When separated on the basis of the peak SYM-H values, 25 % of the CIRs caused the moderate storms, and 5 % caused the intense storms. None of the CIRs caused any super storms (SYM-H ≤ −250 nT). The results are consistent with Alves et al. (2006) who reported that ≈ 33 % of 727 CIRs occurring during 1964-2003 are geoeffective, and only ≈ 2.5 % caused the intense storms. Chi et al. (2018) reported that ≈ 22 % and ≈ 3 % of all CIRs encountered by Wind/ACE during 1995-2016 resulted in the moderate and intense storms at Earth, respectively.

The seasonal and solar cycle dependencies of the CIRs causing geomagnetic storms are shown in Figure 3.9. Figure 3.9b shows the percent of CIRs causing a geomagnetic storm with the SYM-H peak ≤ -50 nT during each month of each year of the entire period of study. Based on this data, the yearly and monthly superposed storm occurrences are shown by histograms in Figures 3.9a and 3.9c, respectively.

During the year 2014 (the solar maximum), $\approx$ 27 % of the 11 CIRs caused geomagnetic storms. During the years (2012-2013) preceding the solar maximum, CIRs occurring during the first half of the years are found to be more geoeffective compared to those occurring during the second half (Figure 3.9b). The reverse is true for the years (2015-2016) following the solar maximum, when geoeffeiveness is higher during the second half of the years. This resulted in an overall semi-annual variation of the geoeffectiveness, showing two peaks around March and October, and minima around January and July (Figure 3.9c). Another interesting feature is that on the both sides of the solar maximum, the geoeffectiveness decreases with the decreasing $F_{10.7}$ solar flux. The yearly CIR geoeffectiveness exhibits a significant correlation (correlation coefficient r = 0.66) with the yearly mean $F_{10.7}$ solar flux.

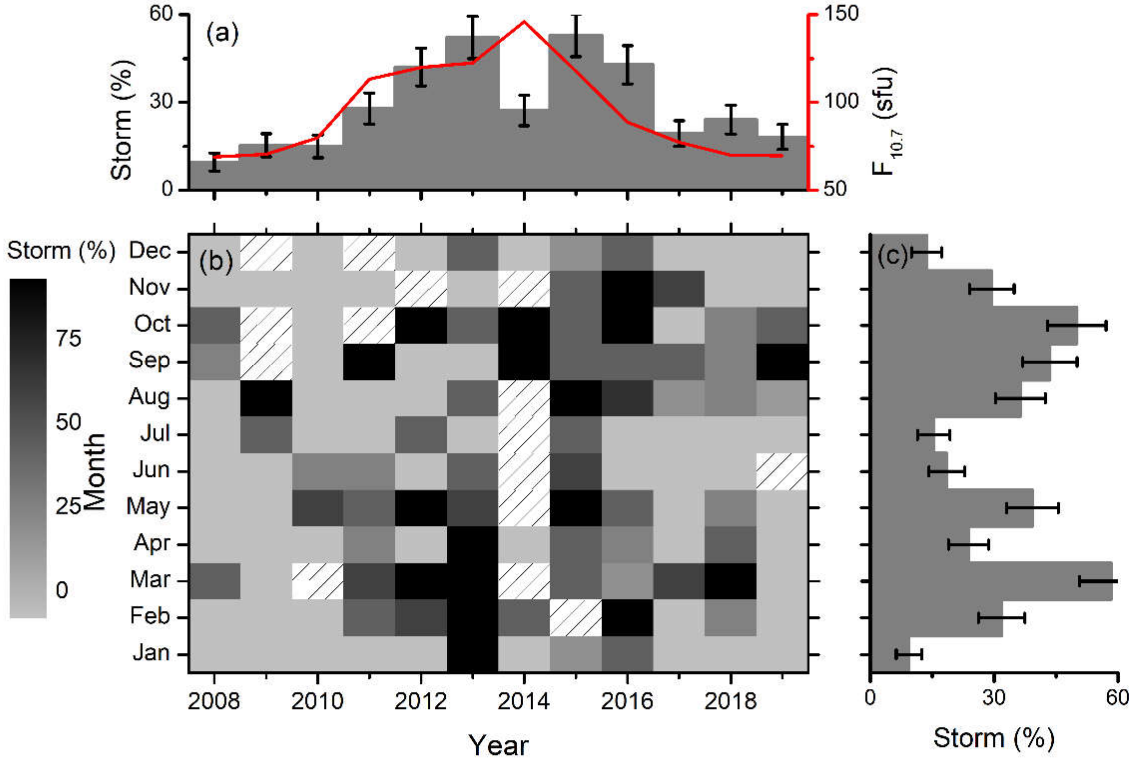

Figure 3.9. Geoeffectiveness of CIRs. (a) Yearly percentage of CIRs causing geomagnetic storms (histograms, legend on the left) with Poisson counting errors (vertical bars), and yearly mean $F_{10.7}$ solar flux (red, legend on the right), (b) year-month contour plot of CIRs causing geomagnetic storms, values of different shading are given in legend on the left, hatching lines indicates intervals with no CIR, (c) monthly percentage of CIRs causing geomagnetic storms with Poisson counting error bars.

No such study of the solar cycle and seasonal variations of the CIR geoeffectiveness was reported before. The seasonal dependence of the CIR geoeffectiveness is consistent with the well-known semi-annual variation of the geomagnetic activity (see Broun, 1848; Sabine, 1852; Baker et al., 1999; Cliver et al., 2000; Kanekal et al., 2010; Danilov et al., 2013; Lockwood et al., 2020; Marques de Souza Franco et al., 2021; Hajra, 2021b, and references therein). This is generally discussed in the context of three mechanisms, namely: (1) the "axial effect" (Cortie, 1912), which is related to the Earth's position in the heliosphere, (2) the "equinoctial effect" (Boller and Stolov, 1970), related to the relative angle of solar wind incidence with respect to the Earth's rotation axis, and (3) the "Russell-McPherron effect" (Russell and McPherron, 1973), related to the geometrical controls of IMFs. However, which of the mechanisms is dominating here is not known at present.

The correlation of the CIR geoeffectiveness with the solar flux is interesting. The exact reason is not known. It may be related to an overall higher value of the solar wind-magnetosphere coupling during the solar maximum, and its decreasing value with the decreasing solar flux (e.g., Hajra, 2021c, and references therein). This should be explored further. Another plausible reason of the enhanced CIR geoeffectiveness during the solar maximum can be the interaction of CIRs with the interplanetary coronal mass ejections (ICMEs) (Chi et al., 2018). ICMEs are the interplanetary remnants of the coronal mass ejections (CMEs; e.g., Illing and Hundhausen, 1986), which can be rotated/modified when propagating through the interplanetary medium (e.g., Odstrcil and Pizzo, 1999; Yurchyshyn et al., 2007; Palmerio et al., 2018). The interplanetary medium is dominated by ICMEs during the solar cycle maximum (e.g., Webb and Howard, 1994; Gopalswamy et al., 2004; Tsurutani et al., 2006; Obridko et al., 2012). Chi et al. (2018) reported a remarkably higher geoeffectiveness of the CIR-ICME combined structures than the isolated CIRs, which seems to be consistent with the present result.

Among all of the 110 sheath events identified in this work, only 20 (i.e., ≈ 18 % of the sheaths) caused geomagnetic storms with the SYM-H peak ≤ −50 nT (Table 3.1). When separated on the basis of the peak SYM-H values, 14 % of the CIRs caused the moderate storms, and 4 % caused the intense storms. None of the sheaths caused any super storms (SYM-H ≤ −250 nT).

The seasonal and solar cycle dependencies of the sheaths causing geomagnetic storms are shown in Figure 3.10. Contour plot Figure 3.10b shows the percent of sheaths causing a geomagnetic storm with the SYM-H peak ≤ −50 nT during each month of each year of the entire period of study. Based on this data, the yearly and monthly superposed storm occurrences by sheaths are shown by histograms in Figures 3.10a and 3.10c, respectively.

From Figure 3.10a it is clear that there is no dependence between sheath geoeffectiveness and solar flux. The maximum yearly percentage of storms were occurred during the year 2015 (≈ 44 %) (after solar maximum) with comparable percentage in 2010, 2017 and 2019 (≈ 28 %, 33 %, 25 % respectively). From the data it is also notable that no storms were caused by sheaths during 2008, 2009 and 2018. Figure 3.10b shows interesting seasonal dependence of storms caused by sheaths. Two peaks were observed during equinoxes (March and September) with a monthly percentage of ≈ 37.5 and ≈ 40 respectively. A comparable percentage was observed during October (≈ 33.3 %). It is interesting that no storms were caused by sheaths during the month of January and February.

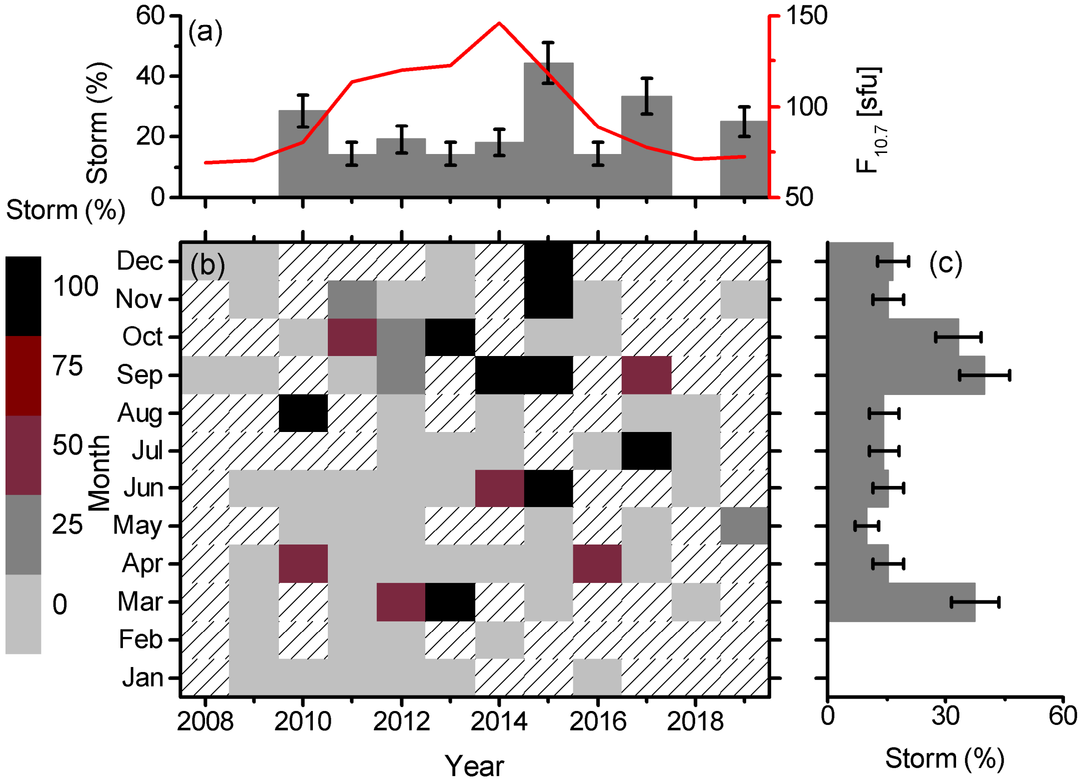

Figure 3.10. Geoeffectiveness of sheaths. (a) Yearly percentage of sheaths causing geomagnetic storms (histograms, legend on the left) with Poisson counting errors (vertical bars), and yearly mean $F_{10.7}$ solar flux (red, legend on the right), (b) year-month contour plot of sheaths causing geomagnetic storms, values of different shading are given in legend on the left, hatching lines indicates intervals with no sheath, (c) monthly percentage of sheaths causing geomagnetic storms with Poisson counting error bars.

Geomagnetic activity during each of the sheaths and CIRs are characterized by the maximum AE and the minimum SYM-H values during the events. Distributions of the AE and SYM-H values for all sheaths and CIRs are shown in Figure 3.11. Their statistical values are summarized in Table 3.1. AE varies from 21 to 2803 nT (57 to 2698 nT) for sheaths (CIRs) with an average AE of 827 nT (1137 nT) for all sheaths (CIRs). The SYM-H index varies between 21 and −152 nT (1 and −223 nT) with an average of

−27 nT (−42 nT) for all sheaths (CIRs). Thus, the average AE activity is ≈ 38 % and the SYM-H activity is ≈ 55 % stronger during CIRs than during the sheaths.

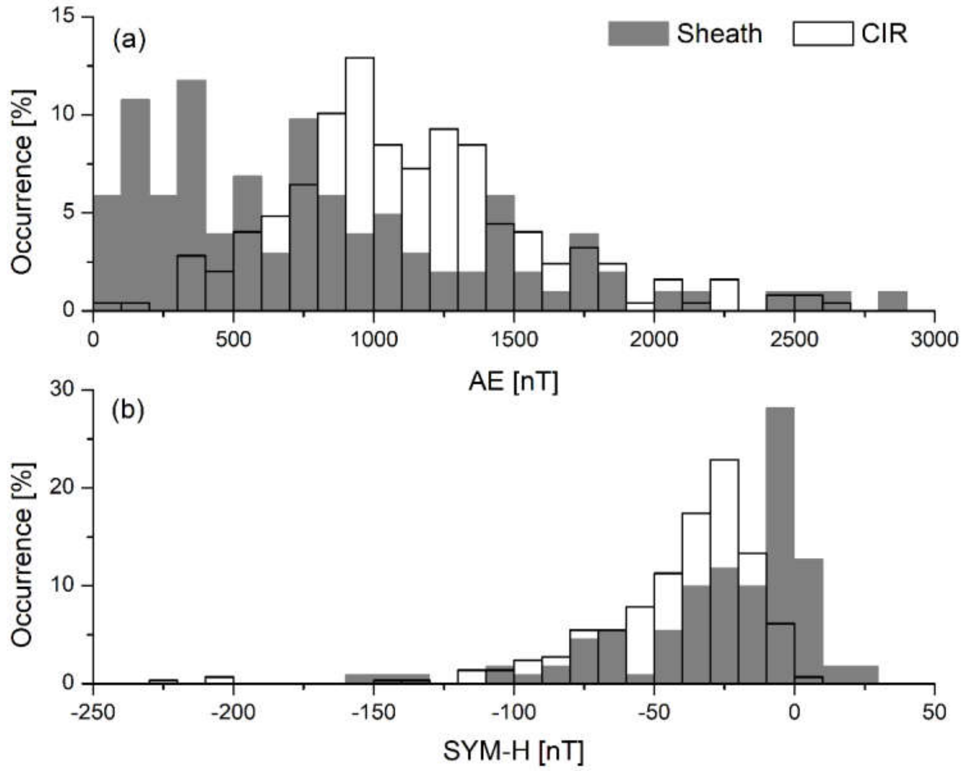

Figure 3.11. Histograms of (a) AE and (b) SYM-H during sheaths (gray) and CIRs (empty).

Table 3.1. Geoeffectiveness of sheaths and CIRs.

Storm type	Sheath	CIR
Moderate (−50 nT ≥ SYM-H > −100 nT)	14 %	25 %
Intense (SYM-H ≤ −100 nT)	4 %	5 %
All (SYM-H ≤ −50 nT)	18 %	30 %

Table 3.1 lists the percent of all sheaths and CIRs causing geomagnetic storms with the minimum SYM-H ≤ −50 nT. While their efficiency in causing intense storm is more or less same, CIRs are found to be more efficient in causing moderate storms than sheaths.

The CIR geoeffectiveness reported in this work is consistent with results reported by Alves, Echer, and Gonzalez (2006) for CIRs during 1964 – 2003, and by Chi et al. (2018) for CIRs during 1995 – 2016. From analysis of all intense geomagnetic storms (with minimum Dst ≤ −100 nT) during Solar Cycle 23, Huttunen and Koskinen (2004) and Echer et al. (2008) concluded that the largest fraction of the storms is caused by the sheaths upstream of the MCs. In fact, a significant number of ICME-related storms are suggsested to be pure sheath induced storms (e.g., Tsurutani et al., 1988; Huttunen et al., 2002; Huttunen and Koskinen, 2004). However, fraction of the all sheaths causing geomagnetic storms and their solar cycle variations is reported in the present work for the first time, to our knowledge.

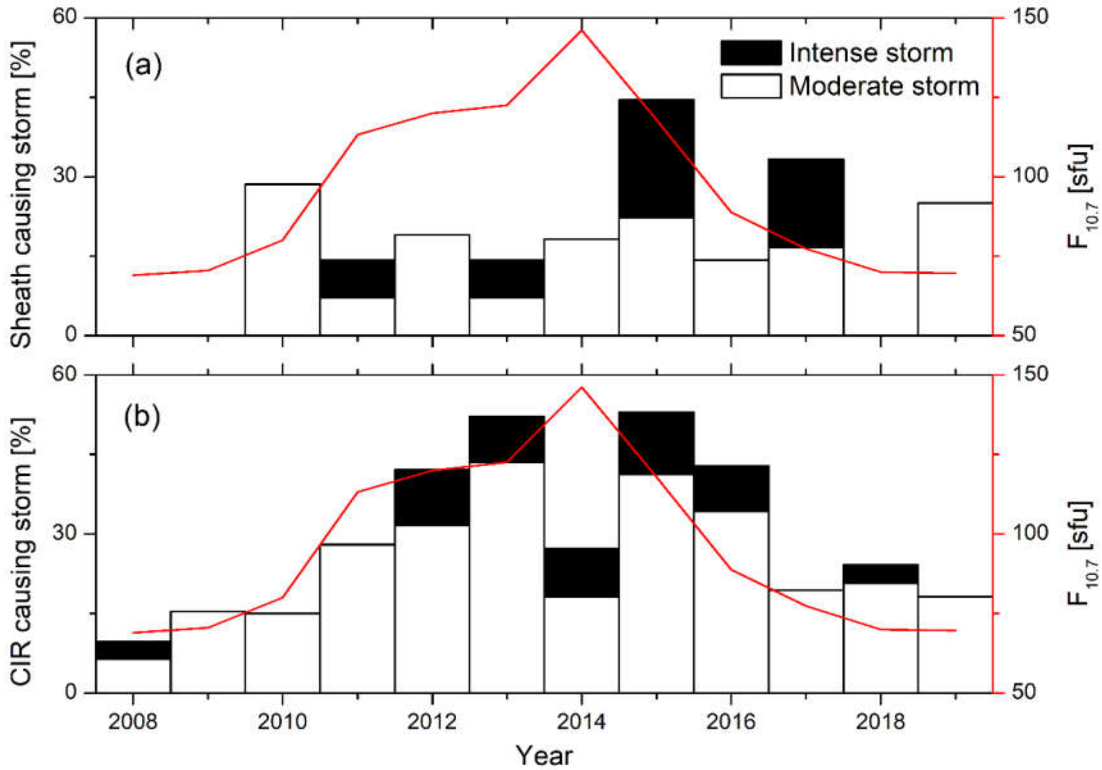

Figure 3.12. Stacked column chart showing percent of (a) sheaths and (b) CIRs causing moderate (empty) and intense storms (black).

Stack histograms in Figure 3.12 shows the percent of sheaths (Figure 3.12a) and CIRs (Figure 3.12b) causing moderate (empty column) and intense storms (black column) in each year of observation. The $F_{10.7}$ solar flux is shown for a reference to the solar cycle.

While the sheath occurrence is well-organized with the solar-flux variation (Figure 3.8), their geoeffectiveness seem to be independent of the solar-cycle phase (Figure 3.12a). On the other hand, the CIR geoeffectiveness is prominently correlated to the solar flux variation, that is, the decreasing CIR geoeffectiveness with the decreasing solar flux (Figure 3.12b). The latter result was attributed to the enhancement of the CIR geoeffectiveness during the solar maximum owing to the CIR-ICME interaction (e.g., Chi et al., 2018; Hajra and Sunny, 2022, and references therein).

3.4. Characteristics of CIRs and sheaths

Figure 3.13 shows histograms of the sheath and CIR characteristic parameters. Based on these distributions, statistical medians, means and standard deviations from the means for all of the sheaths and CIRs are listed in Table 3.2.

The characteristic parameters exhibit a large range of variation for both sheaths and CIRs. For all sheaths (CIRs), the average Vsw varies from ≈ 288 to 761 km s^{-1} (≈ 377 to 719 km s^{-1}) with an average V_{sw} of ≈ 443 km s^{-1} (≈ 495 km s−1) for all events, the peak N_{sw} varies between ≈ 3.3 and 71.9 cm^{-3} (≈ 2.4 and 81.0 cm^{-3}) with an average N_{sw} of ≈ 26.9 cm^{-3} (≈ 29.3 cm^{-3}), the peak P_{sw} varies between ≈ 1.0 and 59.9 nPa (≈ 1.4 and 57.2 nPa) with an average P_{sw} of ≈ 11.0 nPa (≈ 10.5 nPa), the peak T_{sw} varies between ≈ 0.2×10^5 and 45.6×10^5 K (≈ 1.0×10^5 and 26.4×10^5 K) with an average T_{sw} of ≈ 3.7×10^5 K (≈ 4.9×10^5 K), the peak B_0 varies from ≈ 2.9 to 43.8 nT (≈ 4.6 to 44.9 nT) with an average B0 of ≈ 13.4 nT (≈ 14.8 nT), and the minimum B_z varies from ≈ −39.0 to 0.2 nT (≈ −38.7 to −1.8 nT) with an average B_z of ≈ −9.1 nT (≈ −10.9 nT) for all events. Duration of sheaths (CIRs) varies between ≈ 1.33 and 33.58 hours (≈ 2.75 and 82.10 hours) with an average duration of ≈ 11.47 hours (≈ 26.47 hours) for all events. The estimated radial extent of the sheaths (CIRs) is ≈ 0.02 to 0.35 AU (≈ 0.03 to 0.98 AU), with an average extent of ≈ 0.12 AU (≈ 0.31 AU) for all events. As can be found from the standard deviations (Table 3.2), ranges of variations are significantly larger for sheaths than for CIRs.

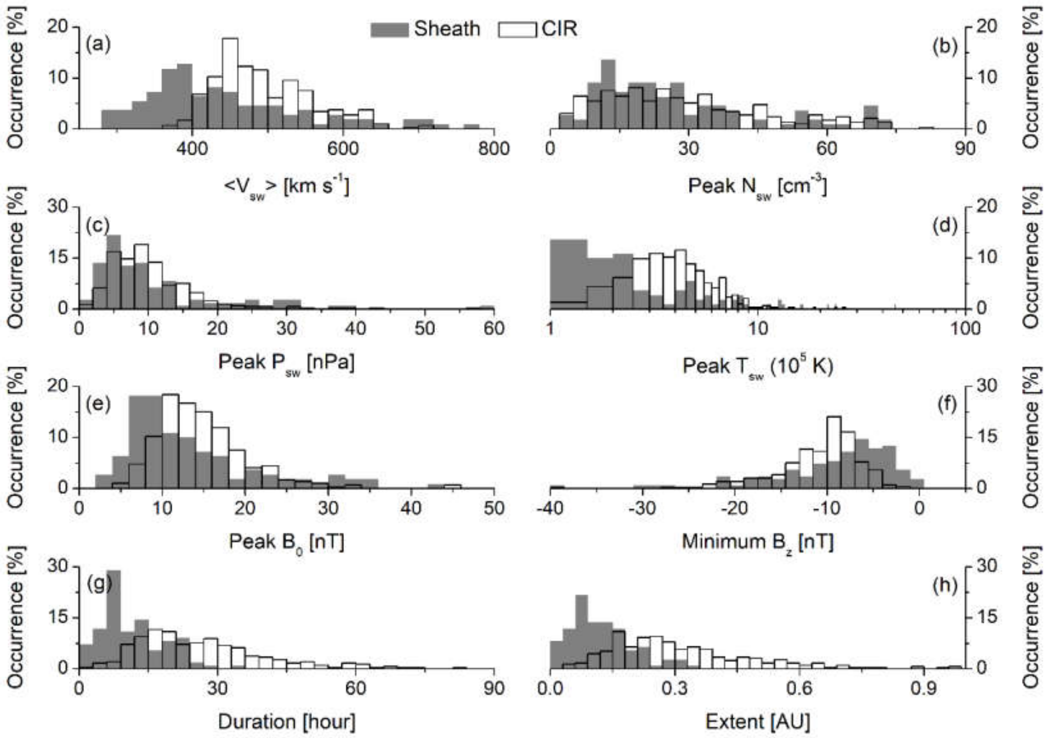

Figure 3.13. Histograms of (a) average V_{sw}, (b) peak N_{sw}, (c) peak P_{sw}, (d) peak T_{sw}, (e) peak B_0, (f) minimum B_z during sheaths and CIRs, and (g) duration, and (h) radial extent of sheaths and CIRs. Gray and empty histograms correspond to sheaths and CIRs, respectively.

Table 3.2. Statistical characteristics and geomagnetic impacts of sheaths and CIRs.

Parameter	Interplanetary sheaths		CIRs		p-value
	Median	Mean ± SD[a]	Median	Mean ± SD[a]	
$< V_{sw} >$ [km s^{-1}]	412	443 ± 106	480	495 ± 65	<0.0001
N_{sw} [cm^{-3}]	22.0	26.9 ± 17.6	25.7	29.3 ± 18.0	0.1855
P_{sw} [nPa]	7.7	11.0 ± 9.6	9.0	10.5 ± 6.7	0.1233
T_{sw} [10^5 K]	1.76	3.70 ± 5.76	4.26	4.91 ± 3.13	<0.0001
B_0 [nT]	10.9	13.4 ± 8.1	13.8	14.8 ± 5.6	<0.0001
B_z [nT]	−7.4	−9.1 ± 6.8	−9.6	−10.9 ± 4.7	<0.0001
Duration [hours]	9.42	11.47 ± 6.70	23.58	26.47 ± 14.09	<0.0001
Radial Extent [AU]	0.11	0.12 ± 0.08	0.27	0.31 ± 0.17	<0.0001
AE [nT]	724	827 ± 643	1072	1137 ± 457	<0.0001
SYM-H [nT]	−18	−27 ± 34	−35	−42 ± 31	<0.0001

[a]SD == standard deviation.

Wu and Lepping (2016) studied 94 sheaths preceded by interplanetary shocks and followed by MCs using in situ Wind measurements during 1995 – 2012. During these sheaths, Kilpua, Koskinen, and Pulkkinen (2017) explored the distributions of solar-wind plasma and IMF parameters measured by Advanced Composition Explorer (ACE) and Wind and time-shifted to the Earth's bow-shock nose. Myllys et al. (2016) also developed distributions of solar-wind parameters during geoeffective sheaths. Kilpua et al. (2019) studied 89 sheaths during Solar Cycles 23 and 24. In general, the sheath characteristic solar-wind plasma parameters and IMF values are comparable with those reported in the present work. Slightly higher plasma speed and stronger southward IMF component reported by Wu and Lepping (2016) could be associated with the fact that the Solar Cycle 24 (present work) is significantly weaker than the previous cycle (see Hajra, 2021c, for a detailed comparison of Solar Cycle 24 with all previous solar cycles in the space age).

The CIR characteristics are comparatively well explored than the sheaths. Alves, Echer, and Gonzalez (2006) studied CIR characteristics using solar-wind measurements shifted to the Earth's bow-shock nose during 1964 – 2003. Jian et al. (2006) used the

ACE and Wind measurements to study CIRs during 1995 – 2004. Jian et al. (2019) explored CIRs encountered by the Solar Terrestrial Relations Observatory (STEREO) spacecraft during 2007 – 2016. The CIR characteristic features obtained by the cited works are found to be more or less consistent with present results (see Hajra and Sunny, 2022, for a complete discussion on this).

From Figure 3.13 and Table 3.2, it can be found that the characteristic solar-wind parameters, duration and radial extent of the CIRs are higher than those of the sheaths, on average. Significance of the statistics is verified by computation of p-values using the median and number of the events, based on the Wilcoxon Rank Sum Test (Nonparametric Statistical Inference by J. D. Gibbons & S. Chakraborti). This test is a nonparametric test for two samples with any distribution (normal or not). The p-values are listed in Table 3.2. The p-value less than 0.05 ($p < 0.05$) indicates that the two means are significantly different (Press et al., 1992). Thus, from the table, we can conclude that sheaths and CIRs are characterized by statistically identical/comparable average N_{sw} and P_{sw} (confirmed by $p > 0.05$), that is, the identical plasma density and ram pressure. However, on average, the CIR has ≈ 12 % higher V_{sw}, ≈ 33 % higher T_{sw}, ≈ 10 % higher IMF B_0 ≈ 131 % longer duration, and ≈ 158 % larger radial extent than the sheath.

3.5. Comparison between geoeffective and non-geoeffective CIRs and sheaths

Geoeffective and Non-geoeffective CIRs

Figure 3.14 shows two CIR events occurring during the year 2013. Solar-wind plasma V_{sw}, N_{sw}, T_{sw}, IMF B_0 and B_Z-component are explored to study the solar-wind and interplanetary condition during the CIRs. From enhanced B_0 and N_{sw}, two CIRs can be identified from ≈ 1625 UT on day 151 to ≈ 0244 UT on day 153 (marked by a light-gray shading), and from ≈ 1546 UT on day 198 to ≈ 0421 UT on day 200 (marked by hatching). The geomagnetic condition is explored by the geomagnetic indices AE and SYM-H. During the first CIR event, the maximum AE value is 1767 nT at ≈ 0357 UT and the minimum SYM-H value is −137 nT at ≈ 0748 UT on day 152. The SYM-H value represents an intense storm (see Gonzalez et al., 1994, for classification of storms based on the ring current intensity). During the second CIR, the maximum AE (1180 nT) and the minimum SYM-H (−13 nT) values indicate that the CIR was non-geoeffective.

From the analysis of the solar-wind and interplanetary parameters, the characteristics of the two CIRs can be compared. The geoeffective (non-geoeffective) CIR event is characterized by a mean V_{sw} of 658 km s^{-1} (465 km s^{-1}), the peak N_{sw} of 35.5 cm^{-3} (21.1 cm^{-3}), T_{sw} of 7.3×10^5 K (6.7×10^5 K) and IMF B_0 of 22.3 nT (18.3 nT). All these parameters have higher values for the geoeffective CIR than the non-geoeffective event. The most prominent difference is recorded in the IMF B_Z-component (Figure 3.14e). While B_Z is strongly fluctuating during both the events, the geoeffective CIR is characterized by a long-duration (6.6 hours) southward IMF with minimum B_Z of −21.2 nT. On the other hand, the non-geoeffective CIR is characterized by short-duration southward IMF component with the minimum B_Z of only −11.3 nT.

To summarize the case studies shown in Figure 3.14, all the solar-wind parameters are stronger during the geoeffective CIR than the non-geoeffective CIR. To study the statistical significance of this result, we separated all 290 CIRs (identified by Hajra and Sunny (2022) during 2008 – 2019) into two groups: geoeffective CIRs causing geomagnetic storms with the SYM-H minimum ≤ -50 nT, and non-geoeffective CIRs with the minimum SYM-H > -50 nT. Among the 290 events, 88 are found to be geoeffective and 202 are non-geoeffective.

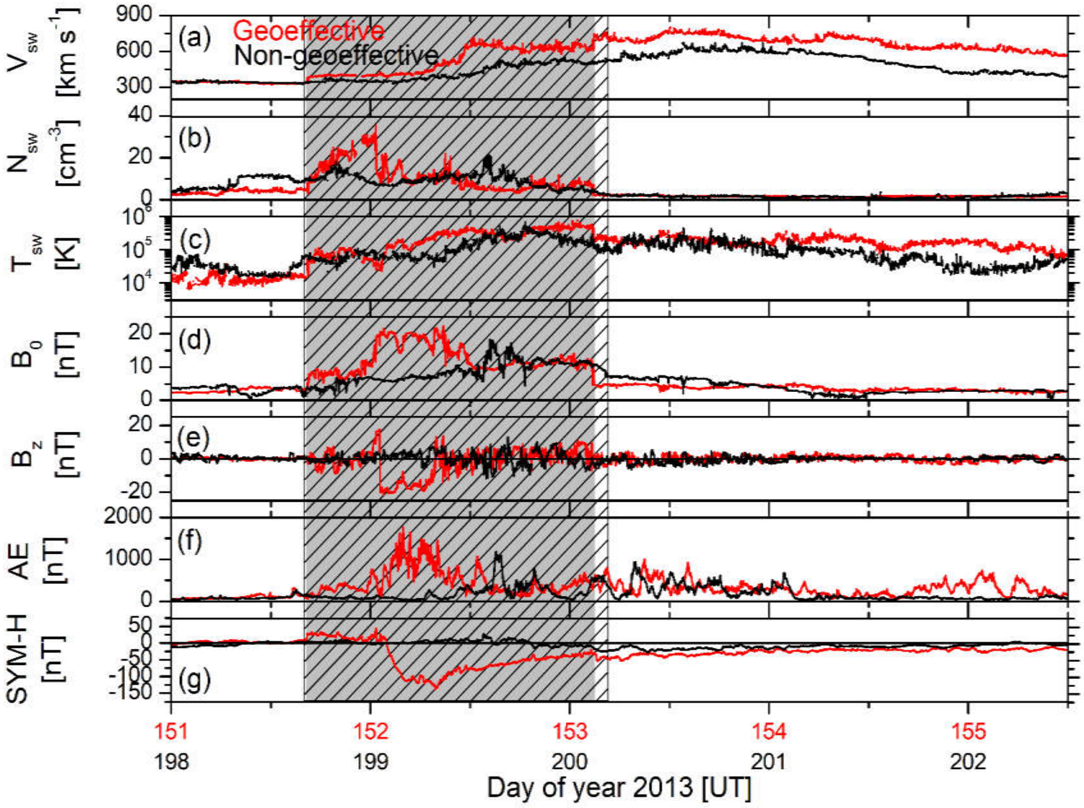

Figure 3.14. Two CIRs during 2013. From top to bottom, the panels show (a) solar-wind plasma speed [V_{sw}], (b) plasma density [N_{sw}], (c) temperature [T_{sw}], (d) IMF magnitude [B_0], (e) IMF B_z, (f) AE, and (g) SYM-H. The geoeffective and non-geoeffective CIR intervals are marked by light-gray shading and hatching, respectively.

Figure 3.15 shows distributions of the CIR characteristic parameters and the peak geomagnetic indices separately during all geoeffective and non-geoeffective CIRs. Based on these distributions, the statistical median, mean and standard deviations are estimated, and listed in Table 3.3. The ranges of the parameters, from the minimum to maximum values for all events, are also listed. Significance of the statistics is verified by computation of p-values using the median and number of the events, based on the Wilcoxon Rank Sum Test (Nonparametric Statistical Inference by J. D. Gibbons & S. Chakraborti). This test is a nonparametric test for two samples with any distribution (normal or not). If the p-value is less than 0.05 for a distribution, the conclusion is that the two means are significantly different (Press et al., 1992).

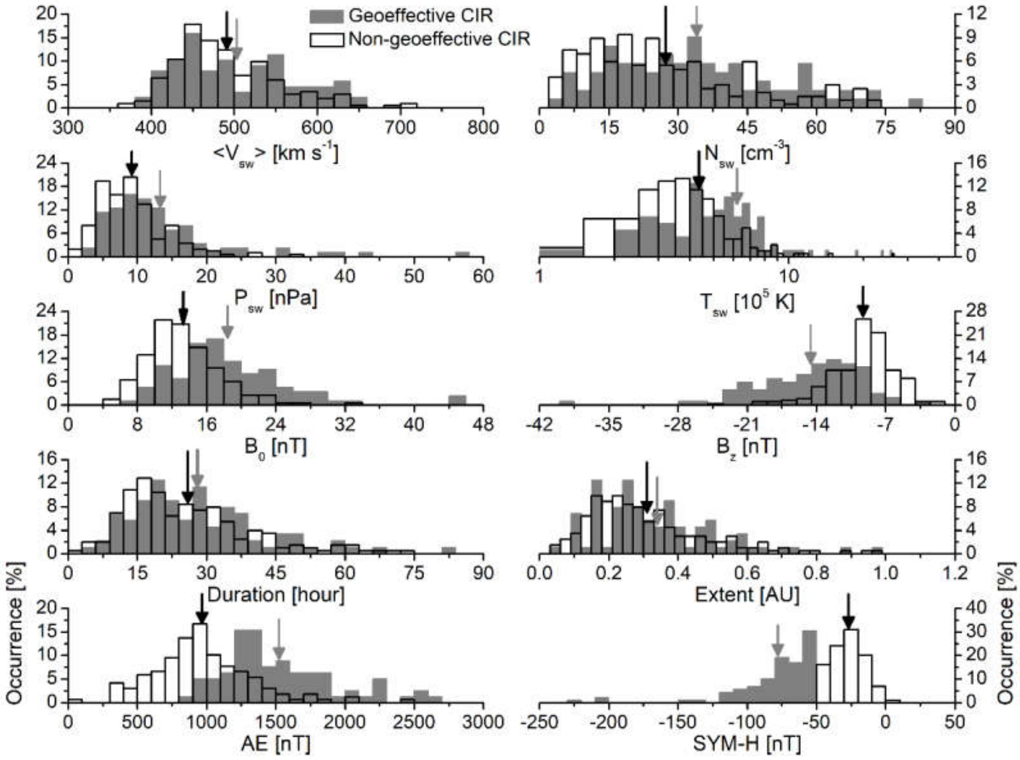

Figure 3.15. Histograms of mean V_{sw}, maximum N_{sw}, P_{sw}, T_{sw}, B_0, and minimum B_z during geoeffective and non-geoeffective CIRs, their duration, and radial extent, maximum AE and minimum SYM-H during geoeffective and non-geoeffective CIRs. Gray and empty histograms correspond to geoeffective and non-geoeffective CIRs, respectively. Downward arrows indicate mean values of the parameters for all geoeffective (gray) and non-geoeffective (black) CIRs.

From the distributions (Figure 3.15), all the parameters are found to exhibit large variations from one event to the other. This is confirmed by large ranges of the parameters, and significantly high standard deviations, ≈ 13 – 68 % of the mean values.

Table 3.3. Statistical characteristics and geomagnetic activity during geoeffective and non-geoeffective CIRs.

Parameter	Geoeffective CIRs			Non-geoeffective CIRs			p-value
	Range[a]	Median	Mean ± SD[b]	Range[a]	Median	Mean ± SD[b]	
$< V_{sw} >$ [km s^{-1}]	[385, 647]	491	503 ± 70	[377, 719]	478	491 ± 63	0.1704
N_{sw} [cm^{-3}]	[4.5, 81.0]	32.5	34.0 ± 18.1	[2.4, 71.9]	23.7	27.3 ± 17.7	0.0016
P_{sw} [nPa]	[3.1, 57.2]	11.3	13.3 ± 9.0	[1.4, 33.6]	8.4	9.2 ± 5.0	<0.0001
T_{sw} [10^5 K]	[1.00, 25.78]	5.54	6.20 ± 3.93	[0.97, 26.35]	3.84	4.36 ± 2.54	<0.0001
B_0 [nT]	[6.6, 44.9]	17.2	18.4 ± 6.7	[4.6, 33.4]	12.8	13.3 ± 4.3	<0.0001
B_z [nT]	[−38.7, −4.0]	−13.7	−14.6 ± 5.5	[−24.0, −1.8]	−8.7	−9.3 ± 3.3	<0.0001
Duration [hours]	[5.25, 82.10]	25.85	28.00 ± 14.65	[2.75, 73.75]	23.05	25.93 ± 13.86	0.2342
Radial Extent [AU]	[0.06, 0.97]	0.30	0.34 ± 0.17	[0.03, 0.98]	0.27	0.31 ± 0.17	0.1093
AE [nT]	[861, 2698]	1409	1523 ± 411	[57, 2451]	926	966 ± 355	<0.0001
SYM-H [nT]	[−38.7, −4.0]	−71	−78 ± 32	[−49, 1]	−26	−27 ± 12	<0.0001

[a]Range == [Minimum, Maximum]; [b]SD == standard deviation.

On average, geoeffective and non-geoeffective CIRs have almost identical duration (≈ 28 and 26 hours, respectively), radial extent (≈ 0.34 and 0.31 AU, respectively), and mean plasma V_{sw} (≈ 503 and 491 km s^{-1}, respectively). As expected, the corresponding p-values are greater than 0.05.

The solar-wind plasma and IMF compressions are found to be significantly stronger during the geoeffective CIRs than the non-geoeffective events (Table 3.3). This is confirmed by p-values less than 0.05. On average, the geoeffective CIRs have ≈ 25 % higher N_{sw}, ≈ 45 % higher P_{sw}, ≈ 42 % higher T_{sw}, ≈ 39 % higher IMF B_0, and ≈ 57 % stronger IMF southward component than the non-geoeffective events.

As a consequence, the auroral electrojet index AE and the ring current index SYM-H are found to be, respectively, ≈ 58 % and ≈ 192 % higher during the geoeffective CIRs than the non-geoeffective events, on average. The average SYM-H (−78 ± 32 nT) and AE (1523 ± 411 nT) for all geoeffective CIRs indicate moderate geomagnetic activity.

Geoeffective and Non-geoeffective Sheaths

Figure 3.16 shows two sheath events occurring during the year 2015 and 2017. Solar-wind plasma V_{sw}, N_{sw}, T_{sw}, IMF B_0 and B_z-component are explored to study the solar-wind and interplanetary condition during the sheaths. From enhanced B_0 and N_{sw}, two sheaths can be identified from ≈ 1834 UT on day 173 to ≈ 0134 UT on day 174 of year 2015 (marked by a light-gray shading), and from ≈ 2348 UT on day 249 to ≈ 0927 UT on day 250 of year 2017 (marked by hatching). The geomagnetic condition is explored by the geomagnetic indices AE and SYM-H. During the sheath in 2015, the maximum AE value is 2698 nT at ≈ 2008 UT and the minimum SYM-H value is −138 nT at ≈ 2015 UT on day 173. The SYM-H value represents an intense storm (see Gonzalez et al., 1994, for classification of storms based on the ring current intensity). During the sheath in 2017, the maximum AE (1430 nT) and the minimum SYM-H (−11 nT) values indicate that the sheath was non-geoeffective.

The characteristics of two sheaths are compared by analyzing solar-wind and interplanetary parameters. The geoeffective (non-geoeffective) sheath event is characterized by a mean V_{sw} of 636 km s^{-1} (549 km s^{-1}), the peak N_{sw} of 71.2 cm^{-3} (15.4 cm^{-3}), T_{sw} of 2.3×10^6 K (1.2×10^6 K) and IMF B_0 of 43.9 nT (15.8 nT). All these parameters have higher values for the geoeffective sheath than the non-geoeffective sheath event. The most prominent difference is recorded in the IMF B_z-component

(Figure 2e). While B_z is strongly fluctuating during both the events, the geoeffective sheath is characterized by a long-duration (1.2 hours) southward IMF with minimum B_z of −38.2 nT. On the other hand, the non-geoeffective sheath is characterized by short-duration southward IMF component with the minimum B_z of only −10.5 nT.

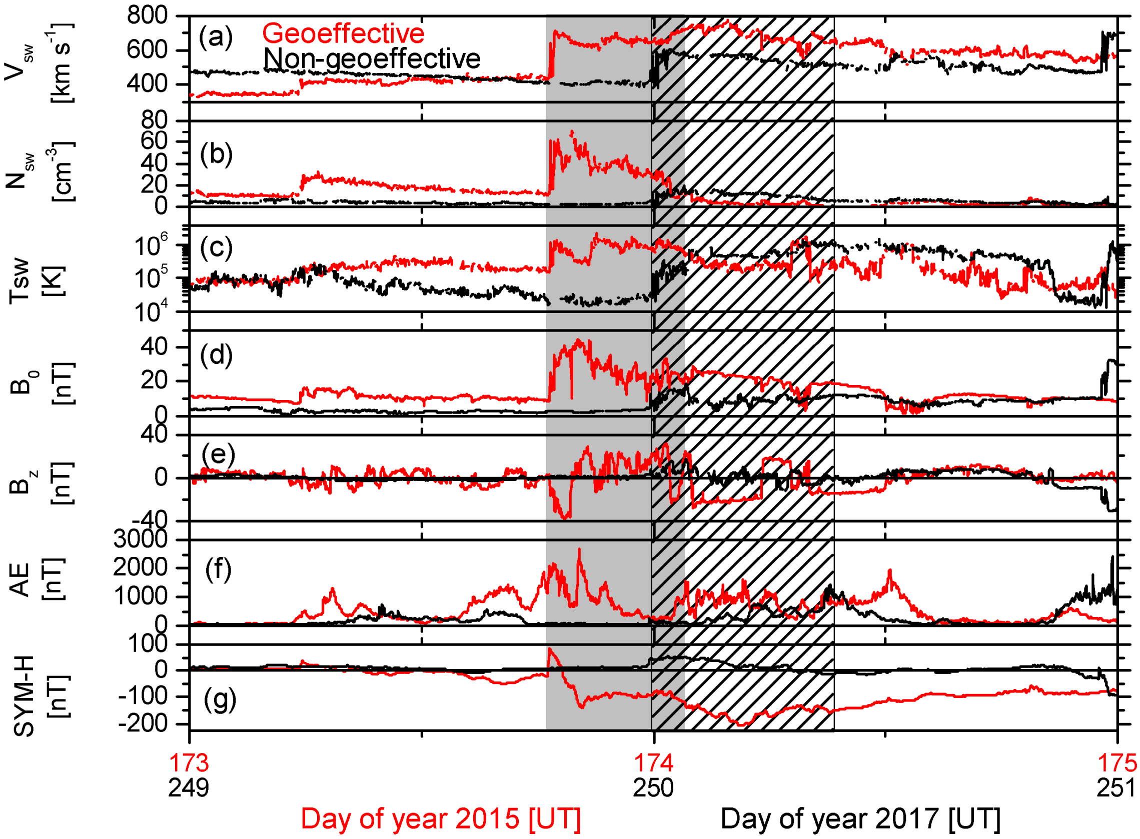

Figure 3.16. Two sheaths during 2015 and 2017. From top to bottom, the panels show (a) solar-wind plasma speed [V_{sw}], (b) plasma density [N_{sw}], (c) temperature [T_{sw}], (d) IMF magnitude [B_0], (e) IMF B_z, (f) AE, and (g) SYM-H. The geoeffective and non-geoeffective sheath intervals are marked by light-gray shading and hatching, respectively.

To summarize the case studies shown in Figure 3.16, all the solar-wind parameters are stronger during the geoeffective sheaths than the non-geoeffective. To study the statistical significance of this result, we separated all 110 sheaths during 2008 –

2019 into two groups: geoeffective sheaths causing geomagnetic storms with the SYM-H minimum ≤ −50 nT, and non-geoeffective sheaths with the minimum SYM-H > −50 nT (as mentioned in the case of geoeffective and non-geoeffective CIRs). Among the 110 events, 20 are found to be geoeffective and 90 are non-geoeffective.

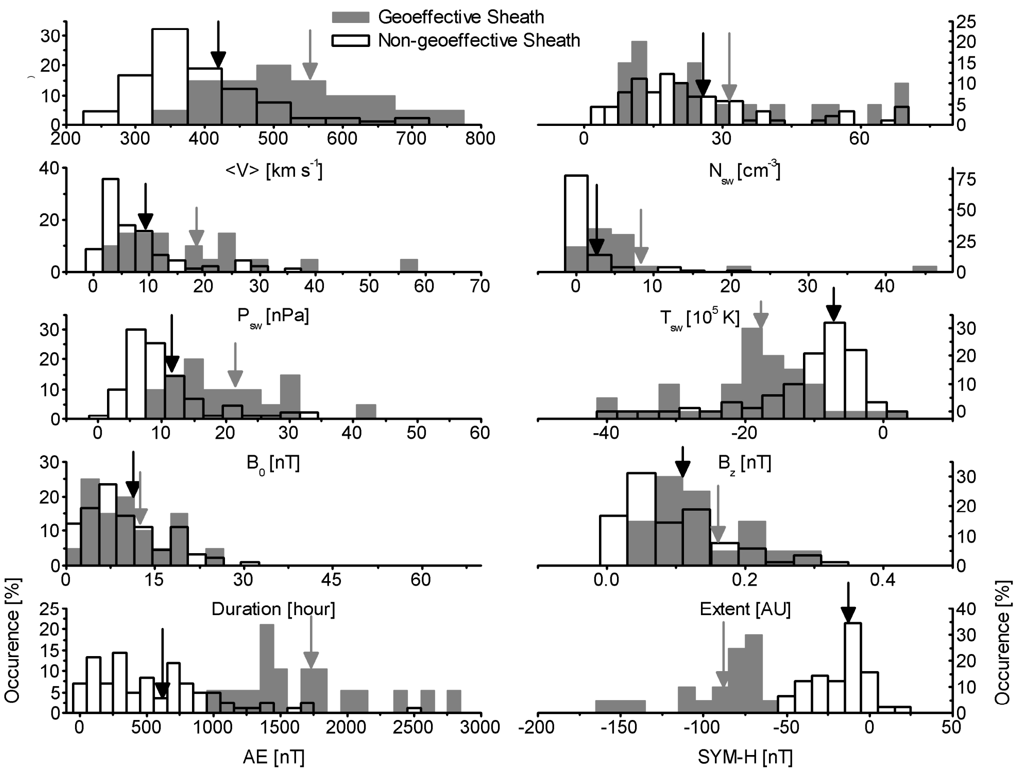

Figure 3.17. Histograms of mean V_{sw}, maximum N_{sw}, P_{sw}, T_{sw}, B_0, and minimum B_z during geoeffective and non-geoeffective sheaths, their duration, and radial extent, maximum AE and minimum SYM-H during geoeffective and non-geoeffective sheaths. Gray and empty histograms correspond to geoeffective and non-geoeffective sheaths, respectively. Downward arrows indicate mean values of the parameters for all geoeffective (gray) and non-geoeffective (black) sheaths

The distribution of sheaths characteristic parameters and the peak geomagnetic indices during geoeffective and non-geoeffective cases are shown in Figure 3.17. Based on these distributions, the statistical median, mean and standard deviations are estimated, and listed in Table 3.4. The ranges of the parameters, from the minimum to maximum values for all events, are also listed. Significance of the statistics is verified by computation of p-values based on the method mentioned above.

Table 3.4. Statistical characteristics and geomagnetic activity during geoeffective and non-geoeffective sheaths.

Parameter	Geoeffective Sheaths			Non-geoeffective Sheaths			p-value
	Range[a]	Median	Mean ± SD[b]	Range[a]	Median	Mean ± SD[b]	
$< V_{sw} >$ [km s^{-1}]	[379, 761]	537	552 ± 111	[288, 715]	399	419 ± 89	<0.0001
N_{sw} [cm^{-3}]	[9.9, 71.9]	26.1	31.5 ± 21.1	[3.3, 71.7]	21.4	25.9 ± 16.7	0.4004
P_{sw} [nPa]	[3.8, 59.9]	13.5	18.6 ± 13.5	[1.0, 37.9]	6.7	9.3 ± 7.7	0.0002
T_{sw} [10^5 K]	[1.50, 45.55]	5.82	8.38 ± 9.97	[0.17, 21.79]	1.4	2.67 ± 3.66	<0.0001
B_0 [nT]	[9.9, 43.8]	19.6	21.5 ± 8.9	[2.9, 34.8]	9.5	11.6 ± 6.7	<0.0001
B_z [nT]	[-39.0, -8.8]	-16.3	-17.7 ± 7.5	[-27.4, 0.2]	-6.4	-7.2 ± 4.9	<0.0001
Duration [hours]	[3.50, 26.65]	11.56	12.40 ± 6.47	[1.33, 33.58]	9.33	11.26 ± 6.77	0.4663
Radial Exent [AU]	[0.06, 0.31]	0.14	0.16 ± 0.07	[0.02, 0.35]	0.10	0.11 ± 0.08	0.0112
AE [nT]	[1031, 2803]	1556	1731 ± 501	[21, 2565]	540	620 ± 471	<0.0001
SYM-H [nT]	[-152, -56]	-80	-88 ± 28	[-49, 21]	-9	-13 ± 16	<0.0001

[a]Range == [Minimum, Maximum]; [b]SD == standard deviation.

On average, geoeffective and non-geoeffective sheaths have almost identical duration (≈ 12 and 11 hours, respectively) and plasma density (≈ 31.5 and 25.9 cm^{-3}, respectively) since p-values are greater than 0.05, but has statistically different radial extent (≈ 0.16 and 0.11 AU, respectively), and mean plasma V_{sw} (≈ 552 and 419 km s^{-1}, respectively).

The solar-wind plasma speed and IMF compressions are found to be significantly stronger during the geoeffective sheaths than the non-geoeffective events (Table 3.4). This is confirmed by p-values less than 0.05. On average, the geoeffective sheaths have ≈ 22 % higher N_{sw}, ≈ 100 % higher P_{sw}, ≈ 211 % higher T_{sw}, ≈ 85 % higher IMF B_0, and ≈ 145 % stronger IMF southward component than the non-geoeffective events.

As a consequence, the auroral electrojet index AE and the ring current index SYM-H are found to be, respectively, ≈ 179 % and ≈ 577 % higher during the geoeffective CIRs than the non-geoeffective events, on average. The average SYM-H (−88 ± 28 nT) and AE (1731 ± 501 nT) for all geoeffective sheaths indicate moderate geomagnetic activity.

Chapter 4

Conclusions and Scope for Future Work

4.1. Conclusions

A database of 290 CIRs and 110 interplanetary sheaths encountered by Earth during January 2008 through December 2019 (solar cycle 24) is developed using upstream solar wind plasma and IMF measurements shifted to the Earth's bow shock nose. The database can be useful for the space research community. The database along with the geomagnetic indices are utilized for a detailed quantitative study on the CIR and sheath characteristics and impacts. The main findings of this work may be summarized as follows.

The conclusions made from the study of all 290 CIR events are:

1) While CIR can occur during any phase of a solar cycle, the occurrence rate is significantly high during the descending phase ($\approx$ 33 year^{-1}) compared to the solar minimum ($\approx$ 24 year^{-1}), the ascending phase ($\approx$ 22 year^{-1}), and the solar maximum ($\approx$ 11 year^{-1}) (Figure 3.6).
2) On average, CIR is characterized by the peak plasma density of $\approx$ 29 cm^{-3}, ram pressure of $\approx$ 11 nPa, temperature of $\approx 5\times10^5$ K, magnetic field magnitude of $\approx$ 15 nT. The solar wind plasma parameters (density, temperature, ram pressure) during the CIR are $\approx$ 4-6 times enhanced compared to their values for the "average" solar winds, while the compression is $\approx$ 3 times in the magnetic field magnitude (Figure 3.13, Table 3.2). The CIR plasma and magnetic field characteristics do not exhibit any prominent solar cycle dependence.
3) CIR is found to be a large-scale interplanetary structure, with an average duration of the order of a day, and an average radial extent of $\approx$ 0.31 AU (Figure 3.13, Table 3.2).
4) Only 30 % of all CIRs under this study are found to be geoeffective in causing the geomagnetic storms with the SYM-H peak ≤ -50 nT (Table 3.1) 25 % caused moderate and 5 % caused intense storms. While the CIR occurrence peaks during

the solar cycle descending phase (Figure 3.6a), the geoeffectiveness of CIR decreases with the decreasing solar flux (Figure 3.12a). The later result is related to an overall decrease in the geoeffectiveness of the solar wind, and solar wind-magnetosphere coupling with the decreasing solar flux. The enhanced CIR geoeffectiveness during the solar maximum may be plausibly associated with the CIR-ICME interactions.

5) While the CIR occurrence does not exhibit any seasonal dependence (Figure 3.6c), geoeffectiveness of CIR exhibits a clear semi-annual variation with two equinoctial peaks and the solstice minima (Figure 3.6c). This result is attributed to the semi-annual variation of the solar wind-magnetosphere coupling efficiency.

The conclusions made from the study of all 110 interplanetary sheath events are:

1) The occurrence rate is high during the ascending phase (≈ 14 year^{-1}) compared to the solar maximum (≈ 11 year^{-1}), the descending phase (≈ 7 year^{-1}), and the solar minimum (≈ 5 year^{-1}).
2) On average, sheath is characterized by the peak plasma density of ≈ 27 cm^{-3}, ram pressure of ≈ 11 nPa, temperature of $\approx 4\times10^{5}$ K, magnetic field magnitude of ≈ 13 nT (Figure 3.13, Table 3.2).
3) The average duration of sheath is of the order of half day (≈ 11.5 hours) and an average radial extent of ≈ 0.12 AU (Figure 3.13, Table 3.2).
4) Only 18 % of all sheaths out of 110 are found to be geoeffective in causing the geomagnetic storms with the SYM-H peak ≤ -50 nT (Table 3.1). 14 % caused moderate storms and 4 % caused intense storms.
5) While the sheath occurrence does not exhibit any seasonal dependence (Figure 3.7c), geoeffectiveness of sheaths exhibits a clear semi-annual variation with two equinoctial peaks in March and September (Figure 3.10c). No storms were caused during January and February. No storms were caused by sheaths during 2008, 2009 and 2018. Figure 3.10

The conclusions made by comparing sheaths and CIRs are:

1) Both sheaths and CIRs represent compressed and turbulent solar-wind plasma and IMF. The turbulence is characterized by enhanced IMF variances (compared to the ambient solar wind), and ≈ 15 minutes- to 1 hour- scale fluctuations as revealed by wavelet and periodogram analyses.
2) While both sheaths and CIRs are compressed plasma regions, their solar wind plasma density and ram pressure are significantly different. On average, the CIRs are ≈ 12 % faster, ≈ 33 % hotter, ≈ 10 % stronger IMF B_0, ≈ 20 % stronger in southward IMF component, ≈ 131 % longer in duration, and ≈ 158 % wider in radial extent than the sheaths.
3) The geomagnetic activity is found to be stronger during the CIRs than the sheaths. The average auroral electrojet index [AE] is ≈ 38 % stronger, and the symmetric ring current index [SYM-H] is ≈ 55 % stronger during the CIRs than the sheaths.
4) Geoeffectiveness of the CIRs is found to be significantly higher than the sheaths. About 25 % of all CIRs and ≈ 14 % of all sheaths caused moderate storms (-50 nT $\geq$ SYM-H > -100 nT). About 5 % of all CIRs and ≈ 4 % of all sheaths caused intense storms (SYM-H ≤ -100 nT).

The conclusions made from studying geoeffective and non-geoeffective CIRs are:

1) On average, geoeffective and non-geoeffective CIRs have almost identical duration (≈ 28 and 26 hours, respectively), radial extent (≈ 0.34 and 0.31 AU, respectively), and mean plasma V_{sw} (≈ 503 and 491 km s^{-1}, respectively).
2) It is found that geoeffective CIR events are characterized by statistically significant higher plasma density, ram pressure, temperature, IMF intensity, and stronger IMF southward component than the non-geoeffective events. The solar-wind plasma and IMF compressions are found to be significantly stronger during the geoeffective CIRs than the non-geoeffective events.
3) On average, the geoeffective CIRs have ≈ 25 % higher N_{sw}, ≈ 45 % higher P_{sw}, ≈ 42 % higher T_{sw}, ≈ 39 % higher IMF B_0, and ≈ 57 % stronger IMF southward component than the non-geoeffective events, the auroral electrojet index AE and

the ring current index SYM-H are found to be, respectively, ≈ 58 % and ≈ 192 % higher during the geoeffective CIRs than the non-geoeffective events. The average SYM-H (−78 ± 32 nT) and AE (1523 ± 411 nT) for all geoeffective CIRs indicate moderate geomagnetic activity.

The conclusions made from studying geoeffective and non-geoeffective sheaths are:

1) On average, geoeffective and non-geoeffective sheaths have almost identical duration (≈ 12 and 11 hours, respectively) and plasma density (≈ 31.5 and 25.9 cm^{-3}, respectively), but has statistically different radial extent (≈ 0.16 and 0.11 AU, respectively), and mean plasma V_{sw} (≈ 552 and 419 km s^{-1} respectively).
2) Geoeffective sheath events are characterized by statistically different ram pressure, temperature, IMF intensity, and stronger IMF southward component than the non-geoeffective events. The solar-wind plasma and IMF compressions are found to be significantly stronger during the geoeffective sheaths than the non-geoeffective events.
3) On average, the geoeffective sheaths have ≈ 22 % higher N_{sw}, ≈ 100 % higher P_{sw}, ≈ 211 % higher T_{sw}, ≈ 85 % higher IMF B_0, and ≈ 145 % stronger IMF southward component than the non-geoeffective events, the auroral electrojet index AE and the ring current index SYM-H are found to be, respectively, ≈ 179 % and ≈ 577 % higher during the geoeffective sheaths than the non-geoeffective events. The average SYM-H (−88 ± 28 nT) and AE (1731 ± 501 nT) for all geoeffective sheaths indicate moderate geomagnetic activity.

4.2. Scope of Future Work

As mentioned before, while both sheaths and CIRs are well explored topics, there are no significant comparative study on their variations, characteristics and geoeffectiveness. Both events are characterized by almost identical plasma and magnetic field compression and turbulence characteristics upstream of the Earth. However, higher geoeffectiveness of the CIRs than the sheaths are reported here for the first time. This is proposed to be caused by enhanced solar wind magnetosphere energy coupling efficiency owing to faster, hotter plasma and stronger southward IMFs during the CIRs. In addition, significantly longer duration and larger radial extent of the CIRs compared to the sheaths seem to be important contributors for enhanced magnetospheric disturbances during the CIRs. A further study on the solar wind-magnetosphere coupling processes during the events can be done to verify the present results.

APPENDIX-A

Table A1. Catalogue of all CIRs under this study. The approximate start and end times at Earth as the day of the year [DOY].

Year	Start [DOY]	End [DOY]	Minimum SYM-H [nT]
2008	5.0	6.3	-32
2008	12.2	13.9	-44
2008	31.5	33.0	-30
2008	41.1	42.1	-35
2008	49.2	50.0	-7
2008	58.6	60.1	-32
2008	68.3	69.8	-100
2008	86.1	87.0	-2
2008	95.3	96.1	-29
2008	113.9	114.7	-45
2008	124.0	125.2	-25
2008	141.7	142.2	-25
2008	144.6	145.3	-26
2008	148.9	149.7	-17
2008	166.6	167.2	-33
2008	171.8	172.5	-18
2008	177.7	177.9	-8
2008	194.0	194.5	-41
2008	204.3	205.0	-8
2008	222.0	223.2	-25
2008	231.0	231.6	-21
2008	247.2	248.6	-66
2008	258.8	259.5	-39
2008	274.7	276.5	-12
2008	285.2	285.9	-65
2008	302.2	303.4	-8
2008	311.9	313.0	-23
2008	330.0	330.5	-8
2008	340.5	341.4	-35
2008	357.3	358.0	-17
2009	1.0	1.2	-11
2009	30.9	31.6	-11
2009	45.1	45.6	-39
2009	57.9	58.7	-31
2009	71.0	72.4	-45
2009	98.7	99.7	-21

Year	Start [DOY]	End [DOY]	Minimum SYM-H [nT]
2009	106.0	107.2	-33
2009	129.0	129.6	-16
2009	179.7	180.4	-38
2009	194.4	195.1	1
2009	203.0	203.5	-94
2009	217.4	218.9	-52
2009	323.7	325.7	-7
2010	11.3	11.8	-10
2010	20.4	21.0	-40
2010	33.6	34.1	-18
2010	49.2	50.0	-23
2010	95.3	95.8	-49
2010	122.2	123.0	-77
2010	138.2	139.9	-35
2010	148.1	150.9	-72
2010	154.6	155.6	-57
2010	166.1	167.2	-37
2010	176.4	178.5	-35
2010	207.7	208.5	-30
2010	222.6	223.2	-19
2010	235.8	236.3	-30
2010	248.7	251.1	-25
2010	266.0	267.4	-36
2010	270.9	271.4	-30
2010	295.4	297.2	-47
2010	322.0	322.9	-13
2010	346.6	346.9	-8
2011	6.8	7.3	-47
2011	13.4	14.0	-25
2011	18.6	19.6	-16
2011	35.1	36.3	-66
2011	45.7	46.1	-49
2011	60.1	61.0	-71
2011	69.3	71.3	-91
2011	80.8	82.5	-17
2011	101.7	102.8	-56
2011	109.9	110.3	-36
2011	119.6	120.3	-37
2011	134.6	137.1	-23
2011	146.6	149.1	-92
2011	155.9	156.4	-58
2011	164.5	165.9	-13
2011	173.1	174.7	-24

Year	Start [DOY]	End [DOY]	Minimum SYM-H [nT]
2011	192.4	193.3	-25
2011	198.7	201.6	-17
2011	205.8	207.0	-28
2011	211.1	212.0	-39
2011	225.8	227.1	-8
2011	234.8	236.1	-15
2011	240.7	241.4	-10
2011	252.5	254.0	-76
2011	332.9	333.4	-28
2012	12.7	13.3	1
2012	15.7	17.2	-23
2012	49.9	50.4	-76
2012	53.1	54.1	-21
2012	57.9	60.1	-58
2012	68.5	69.6	-148
2012	72.4	73.1	-65
2012	75.5	75.9	-77
2012	102.1	104.1	-43
2012	129.7	130.5	-54
2012	154.6	156.8	-41
2012	181.9	182.7	-14
2012	190.4	192.3	-76
2012	205.0	206.3	-17
2012	231.2	232.9	-39
2012	237.3	238.3	-21
2012	263.5	264.6	-42
2012	282.5	284.2	-114
2012	352.1	353.7	-28
2013	25.7	26.9	-60
2013	59.6	61.3	-74
2013	79.4	80.3	-68
2013	87.8	88.9	-63
2013	113.2	115.2	-52
2013	126.2	126.8	-8
2013	144.8	146.3	-63
2013	151.7	153.1	-137
2013	171.1	172.4	-24
2013	178.6	181.1	-106
2013	198.8	200.7	-24
2013	206.5	207.2	-21
2013	216.3	217.2	-52
2013	227.2	228.4	-53
2013	232.8	234.3	-38

Year	Start [DOY]	End [DOY]	Minimum SYM-H [nT]
2013	242.3	243.5	-39
2013	255.5	257.1	-16
2013	281.8	282.1	-76
2013	287.1	288.6	-46
2013	319.6	320.8	-41
2013	341.9	342.4	-72
2013	347.6	350.3	-41
2014	1.3	2.0	-38
2014	12.8	14.3	-23
2014	21.0	22.3	-21
2014	41.7	42.0	-23
2014	50.1	51.8	-119
2014	95.9	96.9	-10
2014	255.7	256.9	-97
2014	293.1	294.3	-50
2014	335.2	336.1	-13
2014	340.2	340.9	-6
2014	345.9	346.8	-33
2015	4.2	5.5	-79
2015	10.3	11.4	-39
2015	21.0	22.4	-18
2015	31.8	33.2	-33
2015	60.9	61.6	-70
2015	64.9	66.5	-36
2015	76.2	77.6	-223
2015	90.4	93.4	-32
2015	104.3	106.3	-81
2015	110.8	111.2	-28
2015	132.7	133.5	-97
2015	138.1	139.6	-62
2015	158.4	159.5	-102
2015	163.6	166.1	-28
2015	173.7	174.5	-206
2015	185.5	186.2	-85
2015	191.8	192.3	-29
2015	203.7	205.3	-80
2015	208.0	208.6	-21
2015	227.4	227.8	-74
2015	230.8	232.0	-51
2015	234.8	235.7	-58
2015	246.5	247.7	-47
2015	251.1	252.7	-112
2015	257.0	257.8	-47

Year	Start [DOY]	End [DOY]	Minimum SYM-H [nT]
2015	263.2	263.5	-81
2015	280.1	280.9	-87
2015	285.3	286.1	-39
2015	307.0	307.5	-57
2015	313.5	314.4	-47
2015	340.8	341.8	-22
2015	343.6	345.0	-16
2015	348.5	348.9	-54
2015	357.2	359.3	-25
2016	5.1	6.1	-21
2016	18.9	21.5	-91
2016	47.1	47.9	-58
2016	66.2	67.2	-107
2016	71.2	71.8	-28
2016	74.7	75.0	-21
2016	86.6	88.1	-11
2016	103.3	104.3	-70
2016	111.8	113.1	-6
2016	113.4	115.1	-18
2016	122.2	124.0	-55
2016	129.0	129.7	-102
2016	135.9	137.0	-34
2016	148.4	149.2	-6
2016	157.3	157.9	-33
2016	162.4	165.2	-21
2016	166.6	167.2	-32
2016	174.4	175.7	-17
2016	188.8	191.1	-32
2016	195.4	196.0	-13
2016	202.0	202.3	-29
2016	210.6	211.3	-40
2016	215.5	216.6	-62
2016	221.3	222.6	-24
2016	236.8	237.5	-83
2016	245.0	246.2	-73
2016	263.8	264.2	-36
2016	268.6	272.0	-51
2016	287.2	288.7	-114
2016	299.3	299.8	-65
2016	315.5	317.4	-54
2016	329.1	330.3	-50
2016	342.5	343.7	-30
2016	355.0	357.1	-50

Year	Start [DOY]	End [DOY]	Minimum SYM-H [nT]
2017	3.3	5.9	-47
2017	18.0	18.7	-22
2017	26.2	27.3	-35
2017	31.1	31.7	-24
2017	35.8	37.5	-13
2017	60.3	60.9	-74
2017	80.0	80.4	-21
2017	86.0	86.9	-86
2017	97.7	98.6	-21
2017	108.6	110.5	-47
2017	135.3	135.9	-14
2017	138.1	139.3	-36
2017	162.5	162.8	-4
2017	167.1	167.7	-20
2017	175.9	176.7	-37
2017	201.2	202.5	-40
2017	215.5	216.6	-28
2017	223.2	224.8	-10
2017	228.1	229.9	-22
2017	243.2	243.5	-62
2017	257.5	257.8	-17
2017	270.0	271.4	-74
2017	283.8	285.2	-47
2017	297.4	298.4	-34
2017	311.1	312.1	-84
2017	319.2	320.4	-36
2017	324.6	325.5	-58
2017	338.7	339.9	-47
2017	345.2	346.3	-23
2017	350.9	351.7	-21
2017	358.1	358.9	-21
2018	8.3	9.1	-21
2018	13.7	14.4	-21
2018	21.1	22.4	-19
2018	47.0	48.1	-17
2018	53.2	54.9	-29
2018	58.0	58.6	-58
2018	77.3	78.1	-50
2018	99.1	100.4	-42
2018	110.0	110.9	-84
2018	125.4	126.1	-65
2018	142.6	143.6	-13
2018	151.6	152.6	-47

Year	Start [DOY]	End [DOY]	Minimum SYM-H [nT]
2018	168.6	169.6	-40
2018	177.1	177.2	-47
2018	201.6	202.6	-21
2018	205.2	205.7	-17
2018	227.0	228.5	-40
2018	231.7	232.4	-28
2018	237.6	238.8	-205
2018	253.4	254.6	-63
2018	260.0	260.8	-13
2018	264.7	265.7	-47
2018	274.4	275.0	-15
2018	280.4	280.8	-53
2018	286.3	287.0	-47
2018	308.6	309.8	-29
2018	313.7	314.5	-45
2018	341.2	343.6	-26
2018	361.9	362.7	-28
2019	4.2	5.4	-25
2019	16.7	17.7	-27
2019	23.0	25.1	-31
2019	44.3	44.7	-25
2019	58.4	59.1	-32
2019	87.2	87.6	-17
2019	94.3	94.9	-32
2019	121.2	122.2	-36
2019	146.9	149.5	-33
2019	189.8	190.3	-25
2019	211.4	213.1	-19
2019	217.0	217.9	-63
2019	221.7	222.5	-28
2019	224.2	225.9	-18
2019	238.8	239.6	-29
2019	242.5	243.6	-43
2019	270.3	271.0	-58
2019	273.4	274.6	-50
2019	282.8	283.4	-39
2019	297.3	298.6	-53
2019	324.9	326.1	-17
2019	352.1	353.4	-35

APPENDIX-B

Table A2. Catalogue of all interplanetary sheaths under this study. The approximate start and end times at Earth as the day of the year [DOY].

Year	Start [DOY]	End [DOY]	Minimum SYM-H [nT]
2008	261.05	261.18	-21
2008	338.40	339.54	-20
2008	351.33	352.14	-9
2009	25.94	26.26	-1
2009	34.84	35.12	-19
2009	70.94	71.06	-8
2009	112.46	112.56	-7
2009	154.60	154.88	-3
2009	178.50	178.83	-1
2009	273.06	273.20	-3
2009	305.14	305.43	-9
2009	318.17	318.48	-16
2009	346.24	346.88	2
2010	1.72	1.97	2
2010	95.34	95.54	-49
2010	101.50	102.08	-67
2010	148.11	148.88	6
2010	172.01	172.29	2
2010	215.74	216.23	-80
2010	303.43	304.08	-8
2011	24.30	24.41	-1
2011	49.07	49.92	-29
2011	88.63	88.94	-3
2011	119.27	119.62	-5
2011	148.05	148.27	-37
2011	155.87	156.12	-32
2011	168.12	168.18	3
2011	181.60	181.78	4
2011	260.17	260.59	-48
2011	278.31	278.43	-7
2011	297.78	298.06	-152
2011	305.39	306.04	-63
2011	311.33	312.24	-1
2011	332.91	333.81	-28
2012	22.25	22.51	-8
2012	45.32	45.88	-31

Year	Start [DOY]	End [DOY]	Minimum SYM-H [nT]
2012	57.91	58.79	-44
2012	68.46	68.83	-40
2012	72.39	72.67	-56
2012	75.54	75.78	-64
2012	114.14	114.73	-9
2012	124.09	125.21	-29
2012	136.10	137.50	-23
2012	168.43	168.95	20
2012	196.72	197.30	-27
2012	225.59	225.83	-8
2012	231.17	231.50	-37
2012	245.03	245.38	4
2012	248.96	249.29	-82
2012	274.48	274.95	-38
2012	282.12	282.65	-99
2012	286.00	286.80	-27
2012	305.64	306.03	7
2012	317.98	318.36	-21
2012	328.92	329.53	-45
2013	17.01	17.57	6
2013	19.72	19.97	-18
2013	76.25	76.60	-107
2013	103.95	104.72	-4
2013	120.41	120.52	-6
2013	157.13	157.65	-19
2013	178.61	179.10	-5
2013	185.73	186.09	4
2013	193.70	194.24	-21
2013	275.08	275.98	-88
2013	312.90	312.98	12
2013	334.87	335.17	-25
2013	348.77	349.71	-37
2013	358.92	359.22	-45
2014	36.59	37.14	-1
2014	46.49	47.03	-17
2014	49.30	49.63	-13
2014	95.38	95.94	-21
2014	110.44	111.36	-36
2014	158.70	159.81	-69
2014	180.79	180.90	3
2014	184.03	184.12	9
2014	231.28	231.72	-7
2014	238.17	239.13	-1

Year	Start [DOY]	End [DOY]	Minimum SYM-H [nT]
2014	255.68	255.95	-73
2015	90.36	90.81	-9
2015	99.10	99.94	-13
2015	126.08	126.74	-28
2015	130.25	130.55	-32
2015	173.78	174.07	-137
2015	250.58	251.06	-79
2015	297.78	298.58	12
2015	310.75	311.28	-106
2015	353.69	354.57	-77
2016	18.92	19.46	-19
2016	104.70	105.40	-41
2016	107.24	108.13	-64
2016	201.98	202.51	-32
2016	286.92	287.26	-7
2016	308.77	309.60	-30
2016	314.29	315.05	-7
2017	103.65	104.05	-5
2017	147.66	147.90	21
2017	197.25	197.99	-65
2017	233.93	234.26	-37
2017	249.99	250.44	-14
2017	250.95	251.10	-145
2018	68.01	68.92	-11
2018	157.49	157.73	2
2018	191.17	191.53	-5
2018	237.10	237.56	-5
2019	130.74	130.99	-9
2019	133.99	134.35	-80
2019	146.93	147.28	4
2019	315.26	315.43	-5

REFERENCES

Allen, R.C., Ho, G.C., Mason, G.M., Li, G., Jian, L.K., Vines, S.K., Schwadron, N.A., Joyce, C.J., Bale, S.D., Bonnell, J.W., Case, A.W., Christian, E.R., Cohen, C.M.S., Desai, M.I., Filwett, R., Goetz, K., Harvey, P.R., Hill, M.E., Kasper, J.C., Korreck, K.E., Lario, D., Larson, D., Livi, R., MacDowall, R.J., Malaspina, D.M., McComas, D.J., McNutt, R., Mitchell, D.G., Paulson, K.W., Pulupa, M., Raoua_, N., Stevens, M.L., Whittlesey, P.L., Wiedenbeck, M.: 2021, Radial Evolution of a CIR: Observations From a Nearly Radially Aligned Event Between Parker Solar Probe and STEREO-A. Geophys. Res. Lett. 48, e2020GL091376. https://doi.org/10.1029/2020GL091376

Allen, R.C., Lario, D., Odstrcil, D., Ho, G.C., Jian, L.K., Cohen, C.M.S., Badman, S.T., Jones, S.I., Arge, C.N., Mays, M.L., Mason, G.M., Bale, S.D., Bonnell, J.W., Case, A.W., Christian, E.R., Dudok de Wit, T., Goetz, K., Harvey, P.R., Henney, C.J., Hill, M.E., Kasper, J.C., Korreck, K.E., Larson, D., Livi, R., MacDowall, R.J., Malaspina, D.M., Mc- Comas, D.J., McNutt, R., Mitchell, D.G., Pulupa, M., Raoua_, N., Schwadron, N., Stevens, M.L., Whittlesey, P.L., Wiedenbeck, M.: 2020, Solar Wind Streams and Stream Interaction Regions Observed by the Parker Solar Probe with Corresponding Observations at 1 au. Astrophys. J. Suppl. 246, 36. https://doi.org/10.3847/1538-4365/ab578f

Alves, M.V., Echer, E., Gonzalez, W.D.: 2006, Geoeffectiveness of corotating interaction regions as measured by Dst index. J. Geophys. Res. Space Phys. 111. https://doi.org/10.1029/2005JA011379

Baker, D.N., Kanekal, S.G., Pulkkinen, T.I., Blake, J.B.: 1999, Equinoctial and solstitial averages of magnetospheric relativistic electrons: A strong semi-annual modulation. Geophys. Res. Lett. 26, 3193. https://doi.org/10.1029/1999GL003638

Belcher, J.W., Davis, L. Jr.: 1971, Large-amplitude Alfven waves in the interplanetary medium, 2. J. Geophys. Res. 76, 3534. https://doi.org/10.1029/JA076i016p03534

Belcher, J.W., Davis, L. Jr.: 1971, Large-amplitude Alfven waves in the interplanetary medium, 2. J. Geophys. Res. 76, 3534. https://doi.org/10.1029/JA076i016p03534

Boller, B.R., Stolov, H.L.: 1970, Kelvin-Helmholtz instability and the semi-annual variation of geomagnetic activity. J. Geophys. Res. 75, 6073. https://doi.org/10.1029/JA075i031p06073

Broun, J.A.: 1848, Observations in magnetism and meteorology made at Makerstoun in Scotland. Trans. Royal Society Edinburgh 18, 401.

Burlaga, L., Sittler, E., Mariani, F., Schwenn, R.: 1981, Magnetic loop behind an interplanetary shock: Voyager, Helios, and IMP 8 observations. Journal of Geophysical Research: Space Physics 86, 6673 https://doi.org/10.1029/JA086iA08p06673

Burlaga, L.F., Behannon, K.W., Hansen, S.F., Pneuman, G.W., Feldman, W.C.: 1978, Sources of magnetic fields in recurrent interplanetary streams. J. Geophys. Res. Space Phys. 83, 4177 https://doi.org/10.1029/JA083iA09p04177

Burlaga, L.F., Klein, L.W., Lepping, R.P., Behannon, K.W.: 1984, Large-scale interplanetary magnetic fields: Voyager 1 and 2 observations between 1 AU and 9.5 AU. J. Geophys. Res. Space Phys. 89, 10659. https://doi.org/10.1029/JA089iA12p10659

Chi, Y., Shen, C., Luo, B., Wang, Y., Xu, M.: 2018, Geoeffectiveness of Stream Interaction Regions From 1995 to 2016. Space Weather 16, 1960. https://doi.org/10.1029/2018SW001894

Cliver, E.W., Kamide, Y., Ling, A.G.: 2000, Mountains versus valleys: Semi-annual variation of geomagnetic activity. J. Geophys. Res. Space Phys. 105, 2413. https://doi.org/10.1029/1999JA900439

Cortie, S.J. A. L.: 1912, Sun-spots and Terrestrial Magnetic Phenomena, 1898{1911: the Cause of the Annual Variation in Magnetic Disturbances. Mon. Not. Royal Astron. Society 73, 52. https://doi.org/10.1093/mnras/73.1.52

Daglis, I.A., Thorne, R.M., Baumjohann, W., Orsini, S.: 1999, The terrestrial ring current: Origin, formation, and decay. Rev. Geophys. 37, 407. https://doi.org/10.1029/1999RG900009

Danilov, A.A., Krymskii, G.F., Makarov, G.A.: 2013, Geomagnetic activity as a reflection of processes in the magnetospheric tail: 1. The source of diurnal and semi-annual variations in geomagnetic activity. Geomag. Aeron. 53, 469. https://doi.org/10.1134/S0016793213040051

Davis, J. C. (2002). Statistics and data analysis in geology. Wiley.

Davis, T.N., Sugiura, M.: 1966, Auroral electrojet activity index AE and its universal time variations. J. Geophys. Res. 71, 785. https://doi.org/10.1029/JZ071i003p00785

Driven Sheaths. J. Geophys. Res. 124, 8208 https://doi.org/10.1029/2019JA026952

Dungey, J.W.: 1961, Interplanetary Magnetic Field and the Auroral Zones. Phys. Rev. Lett. 6, 47. https://doi.org/10.1103/PhysRevLett.6.47

Echer, E., Gonzalez, W.D., Guarnieri, F.L., Dal Lago, A., Vieira, L.E.A.: 2005, Introduction to space weather. Adv. Space Res. 35, 855, https://doi.org/10.1016/j.asr.2005.02.098

Echer, E., Gonzalez, W.D., Tsurutani, B.T. and Gonzalez, A.C., 2008. Interplanetary conditions causing intense geomagnetic storms (Dst≤− 100 nT) during solar cycle 23 (1996–2006). Journal of Geophysical Research: Space Physics, 113(A5) https://doi.org/10.1029/2007JA012744

Echer, E., Tsurutani, B.T., Gonzalez, W.D., Kozyra, J.U.: 2011, High Speed Stream Properties and Related Geomagnetic Activity During the Whole Heliosphere Interval (WHI): 20 March to 16 April 2008. Solar Phys. 274, 303. https://doi.org/10.1007/s11207-011-9739-0

Fairfield, D.H. and Cahill Jr, L.J., 1966. Transition region magnetic field and polar magnetic disturbances. Journal of Geophysical Research, 71(1), pp.155-169.

Frank, L.A.: 1967, On the extra-terrestrial ring current during geomagnetic storms. J. Geophys. Res. 72, 3753. https://doi.org/10.1029/JZ072i015p03753

Gardner, L., Sojka, J.J., Schunk, R.W., Heelis, R.: 2012, Changes in thermospheric temperature induced by high-speed solar wind streams. J. Geophys. Res. Space Phys. 117, A12303. https://doi.org/10.1029/2012JA017892

Gazis, P.R., McDonald, F.B., Burger, R.A., Chalov, S., Decker, R.B., Dwyer, J., Intriligator, D.S., Jokipii, J.R., Lazarus, A.J., Mason, G.M., Pizzo, V.J., Potgieter, M.S., Richardson, I.G., Lanzerotti, L.J.: 1999, Corotating Interaction Regions in the Outer Heliosphere. Space Sci. Rev. 89, 269. https://doi.org/10.1023/A:1005270027347

Geophysical Research: Space Physics 87, 613 https://doi.org/10.1029/JA087iA02p00613

Gibbons, J.D. and Chakraborti, S., 2014. Nonparametric statistical inference. CRC press.

Gonzalez, W.D. and Tsurutani, B.T., 1987. Criteria of interplanetary parameters causing intense magnetic storms ($Dst<-100$ nT). Planetary and Space Science, 35(9), pp.1101-1109.

Gonzalez, W.D., Joselyn, J.A., Kamide, Y., Kroehl, H.W., Rostoker, G., Tsurutani, B.T., Vasyliunas, V.M.: 1994, What is a geomagnetic storm? J. Geophys. Res. Space Phys. 99, 5771. https://doi.org/10.1029/93JA02867

Gopalswamy, N., 2016. History and development of coronal mass ejections as a key player in solar terrestrial relationship. Geoscience Letters, 3(1), pp.1-18. https://doi.org/10.1186/s40562-016-0039-2

Gopalswamy, N., Nunes, S., Yashiro, S., Howard, R.A.: 2004, Variability of solar eruptions during cycle 23. Adv. Space Res. 34, 391. DOI 10.1016/j.asr.2003.10.054.

Gosling, J.T. (1990). Coronal Mass Ejections and Magnetic Flux Ropes in Interplanetary Space. In Physics of Magnetic Flux Ropes (eds C.T. Russell, E.R. Priest and L.C. Lee). https://doi.org/10.1029/GM058p0343

Gosling, J.T. and McComas, D.J., 1987. Field line draping about fast coronal mass ejecta: A source of strong out-of-the-ecliptic interplanetary magnetic fields. Geophysical Research Letters, 14(4), pp.355-358.

Gosling, J.T., Baker, D.N., Bame, S.1., Feldman, W.C., Zwickl, R.D. and Smith, E.J., 1987. Bidirectional solar wind electron heat flux events. Journal of Geophysical Research: Space Physics, 92(A8), pp.8519-8535.

Gosling, J.T., Hundhausen, A.J., Bame, S.J.: 1976, Solar wind stream evolution at large heliocentric distances: Experimental demonstration and the test of a model. J. Geophys. Res. 81, 2111. https://doi.org/10.1029/JA081i013p02111

Gosling, J.T., Pizzo, V. and Bame, S.J., 1973. Anomalously low proton temperatures in the solar wind following interplanetary shock waves—evidence for magnetic bottles? Journal of Geophysical Research, 78(13), pp.2001-2009.

Gosling, J.T., Pizzo, V. and Bame, S.J., 1973. Anomalously low proton temperatures in the solar wind following interplanetary shock waves—evidence for magnetic bottles. Journal of Geophysical Research, 78(13), pp.2001-2009.

Grandin, M., Aikio, A.T., Kozlovsky, A.: 2019, Properties and Geoe_ectiveness of Solar Wind High-Speed Streams and Stream Interaction Regions During Solar Cycles 23 and 24. J. Geophys. Res. Space Phys. 124, 3871. https://doi.org/10.1029/2018JA026396

Hajra, R. and Tsurutani, B.T., 2018. Interplanetary shocks inducing magnetospheric supersubstorms (SML<− 2500 nT): unusual auroral morphologies and energy flow. The Astrophysical Journal, 858(2), p.123. https://doi.org/10.3847/1538-4357/aabaed

Hajra, R., Echer, E., Tsurutani, B.T., Gonzalez, W.D.: 2013, Solar cycle dependence of High- Intensity Long-Duration Continuous AE Activity (HILDCAA) events, relativistic electron predictors? J. Geophys. Res. Space Phys. 118, 5626. https://doi.org/10.1002/jgra.50530

Hajra, R., Henri, P., Myllys, M., H_eritier, K.L., Galand, M., Simon Wedlund, C., Breuillard, H., Behar, E., Edberg, N.J.T., Goetz, C., Nilsson, H., Eriksson, A.I., Goldstein, R., Tsurutani, B.T., Mor_e, J., Valli_eres, X., Wattieaux, G.: 2018, Cometary plasma response to interplanetary corotating interaction regions during 2016 June {September: a quantitative study by the Rosetta Plasma Consortium. Mon. Not. Royal Astron. Society 480, 4544. https://doi.org/10.1093/mnras/sty2166

Hajra, R., Henri, P., Myllys, M., H_eritier, K.L., Galand, M., Simon Wedlund, C., Breuillard, H., Behar, E., Edberg, N.J.T., Goetz, C., Nilsson, H., Eriksson, A.I., Goldstein, R., Tsurutani, B.T., Mor_e, J., Valli_eres, X., Wattieaux, G.: 2018, Cometary plasma response to interplanetary corotating interaction regions during 2016 June {September: a quantitative study by the Rosetta Plasma Consortium. Mon. Not. Royal Astron. Society 480, 4544. https://doi.org/10.1093/mnras/sty2166

Hajra, R., Marques de Souza Franco, A., Echer, E., & Bolzan, M. J. A. (2021). Long-term variations of the geomagnetic activity: A comparison between the strong and weak solar activity cycles and implications for the space climate. Journal of Geophysical Research: Space Physics, 126, e2020JA028695. https://doi.org/10.1029/2020JA028695

Hajra, R., Sunny, J.V.: 2022, Corotating Interaction Regions during Solar Cycle 24: A Study on Characteristics and Geoeffectiveness. Solar Phys. 297, 30 https://doi.org/10.1007/s11207-022-01962-1

Hajra, R., Tsurutani, B, T., and Lakhina, G, S (2020). The complex space weather events of 2017 september. The Astrophysiacl Journal, 899 https://doi.org/10.3847/1538-4357/aba2c5

Hajra, R., Tsurutani, B.T., Brum, C.G.M., Echer, E.: 2017, High-speed solar wind stream effects on the topside ionosphere over Arecibo: A case study during solar minimum. Geophys. Res. Lett. 44, 7607. https://doi.org/10.1002/2017GL073805

Hajra, R., Tsurutani, B.T., Echer, E., Gonzalez, W.D., Brum, C.G.M., Vieira, L.E.A., Santolik, O.: 2015b, Relativistic electron acceleration during HILDCAA events: are precursor CIR magnetic storms important? Earth Planet Space 67, 109. https://doi.org/10.1186/s40623-015-0280-5

Hajra, R., Tsurutani, B.T., Echer, E., Gonzalez, W.D., Santolik, O.: 2015a, Relativistic (E> 0.6, > 2.0, and > 4.0 MeV) electron acceleration at geosynchronous orbit during highintensity, long-duration, continuous AE activity (HILDCAA) events. Astrophys. J. 799, 39. https://doi.org/10.1088/0004-637x/799/1/39

Hajra, R., Tsurutani, B.T., Echer, E., Gonzalez, W.D.: 2014a, Relativistic electron acceleration during high-intensity, long-duration, continuous AE activity (HILDCAA) events: Solar cycle phase dependences. Geophys. Res. Lett. 41, 1876. https://doi.org/10.1002/2014GL059383

Hajra, R., Tsurutani, B.T., Lakhina, G.S.: 2020, The Complex Space Weather Events of 2017 September. Astrophys. J. 899, 3. DOI 10.3847/1538-4357/aba2c5.

Hajra, R.: 2021a, Variation of the Interplanetary Shocks in the Inner Heliosphere. Astrophys. J. 917, 91. https://doi.org/10.3847/1538-4357/ac0897

Hajra, R.: 2021b, Seasonal dependence of the Earth's radiation belt - new insights. Ann. Geophys. 39, 181. DOI 10.5194/angeo-39-181-2021.

Hajra, R.: 2021b, Seasonal dependence of the Earth's radiation belt - new insights. Ann. Geophys. 39, 181. https://doi.org/10.5194/angeo-39-181-2021

Hajra, R.: 2021c, Weakest Solar Cycle of the Space Age: A Study on Solar Wind-Magnetosphere Energy Coupling and Geomagnetic Activity. Solar Phys. 296, 33. https://doi.org/10.1007/s11207-021-01774-9

Hamilton, D.C., Gloeckler, G., Ipavich, F.M., Studemann, W., Wilken, B., Kremser, G.: 1988, Ring current development during the great geomagnetic storm of February 1986. J. Geophys. Res. Space Phys. 93, 14343. https://doi.org/10.1029/JA093iA12p14343

Hirshberg, J., Alksne, A., Colburn, D.S., Bame, S.J. and Hundhausen, A.J., 1970. Observation of a solar flare induced interplanetary shock and helium-enriched driver gas. Journal of Geophysical Research, 75(1), pp.1-15.

Hundhausen, A.J., Gosling, J.T.: 1976, Solar wind structure at large heliocentric distances: An interpretation of Pioneer 10 observations. J. Geophys. Res. 81, 1436. https://doi.org/10.1029/JA081i007p01436

Huttunen, K.E.J. and Koskinen, H.E.J., 2004, April. Importance of post-shock streams and sheath region as drivers of intense magnetospheric storms and high-latitude activity. In Annales Geophysicae (Vol. 22, No. 5, pp. 1729-1738). Copernicus GmbH. https://doi.org/10.5194/angeo-22-1729-2004

Huttunen, K.E.J., Koskinen, H.E., Pulkkinen, T.I., Pulkkinen, A., Palmroth, M., Reeves, E.G.D. and Singer, H.J., 2002. April 2000 magnetic storm: Solar wind driver and magnetospheric response. Journal of Geophysical Research: Space Physics, 107(A12), pp.SMP-15. https://doi.org/10.1029/2001JA009154

Illing, R.M.E., Hundhausen, A.J.: 1986, Disruption of a coronal streamer by an eruptive prominence and coronal mass ejection. J. Geophys. Res. Space Phys. 91, 10951. https://doi.org/10.1029/JA091iA10p10951

Iyemori, T., Takeda, M., Nose, M., Odagi, Y., Toh, H.: 2010, Mid-latitude Geomagnetic Indices ASY and SYM for 2009 (Provisional). http://wdc.kugi.kyoto-u.ac.jp/aeasy/asy.pdf

Jian, L., Russell, C.T., Luhmann, J.G., Skoug, R.M.: 2006, Properties of Stream Interactions at One AU During 1995 - 2004. Solar Phys. 239, 337. https://doi.org/10.1007/s11207-006-0132-3

Jian, L.: 2008, PhD thesis, Univ. California Los Angeles.

Jian, L.K., Luhmann, J.G., Russell, C.T., Galvin, A.B.: 2019, Solar Terrestrial Relations Observatory (STEREO) Observations of Stream Interaction Regions in 2007 - 2016: Relationship with Heliospheric Current Sheets, Solar Cycle Variations, and Dual Observations. Solar Phys. 294, 31. https://doi.org/10.1007/s11207-019-1416-8

Jian, L.K., Russell, C.T., Luhmann, J.G., MacNeice, P.J., Odstrcil, D., Riley, P., Linker, J.A., Skoug, R.M., Steinberg, J.T.: 2011, Comparison of Observations at ACE and Ulysses with Enlil Model Results: Stream Interaction Regions During Carrington Rotations 2016{2018. Solar Phys. 273, 179. https://doi.org/10.1007/s11207-011-9858-7

Jian, L.K., Russell, C.T., Luhmann, J.G., Skoug, R.M., Steinberg, J.T.: 2008a, Stream Interactions and Interplanetary Coronal Mass Ejections at 0.72 AU. Solar Phys. 249, 85. https://doi.org/10.1007/s11207-008-9161-4

Jian, L.K., Russell, C.T., Luhmann, J.G., Skoug, R.M.: 2008b, Evolution of solar wind structures from 0.72 to 1 AU. Adv. Space Res. 41, 259. https://doi.org/10.1016/j.asr.2007.03.023

Kanekal, S.G., Baker, D.N., McPherron, R.L.: 2010, On the seasonal dependence of relativistic electron uxes. Ann. Geophys. 28, 1101. https://doi.org/10.5194/angeo-28-1101-2010

Kennel, C.F., Edmiston, J.P., Hada, T.: 1985, A Quarter Century of Collisionless Shock Research, American Geophysical Union (AGU), 1. ISBN 9781118664032 https://doi.org/10.1029/GM034p0001

Kilpua, E., Koskinen, H.E.J., Pulkkinen, T.I.: 2017, Coronal mass ejections and their sheath regions in interplanetary space. Liv. Rev. Solar Phys. 14, 5. https://doi.org/10.1007/s41116-017-0009-6

Kilpua, E.K.J., Fontaine, D., Moissard, C., Ala-Lahti, M., Palmerio, E., Yordanova, E., Good, S.W., Kalliokoski, M.M.H., Lumme, E., Osmane, A., Palmroth, M., Turc, L.: 2019, Solar Wind Properties and Geospace Impact of Coronal Mass Ejection-Driven Sheath Regions: Variation and Driver Dependence. Space Weather 17, 1257 https://doi.org/10.1029/2019SW002217

Kilpua, E.K.J., Hietala, H., Koskinen, H.E.J., Fontaine, D. and Turc, L., 2013, September. Magnetic field and dynamic pressure ULF fluctuations in coronal-mass-ejection-driven sheath regions. In Annales Geophysicae (Vol. 31, No. 9, pp. 1559-1567). Copernicus GmbH. https://doi.org/10.5194/angeo-31-1559-2013

Klein, L.W. and Burlaga, L.F., 1982. Interplanetary magnetic clouds at 1 AU. Journal of Geophysical Research: Space Physics, 87(A2), pp.613-624.

Klein, L.W., Burlaga, L.F.: 1982, Interplanetary magnetic clouds At 1 AU. Journal of526
Krieger, A.S., Timothy, A.F., Roelof, E.C.: 1973, A coronal hole and its identification as the source of a high velocity solar wind stream. Solar Phys. 29, 505. https://doi.org/10.1007/BF00150828

Landau, L.D., Lifshitz, E.M.: 1960, Electrodynamics of Continuous Media, 2nd edn. Pergamon Press, New York. ISBN 9780080570600.

Lei, J., Thayer, J.P., Wang, W., McPherron, R.L.: 2011, Impact of CIR Storms on Thermosphere Density Variability during the Solar Minimum of 2008. Solar Phys. 274, 427. https://doi.org/10.1007/s11207-010-9563-y

Lepping, R.P., Jones, J.A. and Burlaga, L.F., 1990. Magnetic field structure of interplanetary magnetic clouds at 1 AU. Journal of Geophysical Research: Space Physics, 95(A8), pp.11957-11965.

Lockwood, M., Owens, M.J., Barnard, L.A., Haines, C., Scott, C.J., McWilliams, K.A., Coxon, J.C.: 2020, Semi-annual, annual and Universal Time variations in the magnetosphere and in geomagnetic activity: 1. Geomagnetic data. J. Space Weather Space Clim. 10, 23. https://doi.org/10.1051/swsc/2020023

Lomb, N.R., 1976. Least-squares frequency analysis of unequally spaced data. Astrophysics and space science, 39(2), pp.447-462 https://doi.org/10.1007/BF00648343

Marques de Souza Franco, A., Hajra, R., Echer, E., Bolzan, M.J.A.: 2021, Seasonal features of geomagnetic activity: a study on the solar activity dependence. Ann. Geophys. 39, 929. https://doi.org/10.5194/angeo-39-929-2021

Marques de Souza, A., Echer, E., Bolzan, M.J.A. and Hajra, R., 2018, February. Cross-correlation and cross-wavelet analyses of the solar wind IMF B z and auroral electrojet index AE coupling during HILDCAAs. In Annales Geophysicae (Vol. 36, No. 1, pp. 205-211). Copernicus GmbH. https://doi.org/10.5194/angeo-36-205-2018

Moissard, C., Fontaine, D., Savoini, P.: 2019, A Study of Fluctuations in Magnetic Cloud-538

Montgomery, D. and Joyce, G., 1974. Statistical mechanics of “negative temperature” states. The Physics of Fluids, 17(6), pp.1139-1145.

Myllys, M., Kilpua, E.K.J., Lavraud, B., Pulkkinen, T.I.: 2016, Solar wind-magnetosphere coupling efficiency during ejecta and sheath-driven geomagnetic storms. J. Geophys. Res. 121, 4378 https://doi.org/10.1002/2016JA022407

Nakagawa, Y., Nozawa, S., Shinbori, A.: 2019, Relationship between the low-latitude coronal hole area, solar wind velocity, and geomagnetic activity during solar cycles 23 and 24. Earth Planet Space 71, 24. https://doi.org/10.1186/s40623-019-1005-y

Obridko, V.N., Ivanov, E.V., Ozguc, A., Kilcik, A., Yurchyshyn, V.B.: 2012, Coronal Mass Ejections and the Index of E_ective Solar Multipole. Solar Phys. 281, 779. https://doi.org/10.1007/s11207-012-0096-4

Odstrcil, D., Pizzo, V.J.: 1999, Three-dimensional propagation of coronal mass ejections (CMEs) in a structured solar wind ow: 1. CME launched within the streamer belt. J. Geophys. Res. Space Phys. 104, 483. https://doi.org/10.1029/1998JA900019

Palmerio, E., Kilpua, E.K.J., Mostl, C., Bothmer, V., James, A.W., Green, L.M., Isavnin, A., Davies, J.A., Harrison, R.A.: 2018, Coronal Magnetic Structure of Earthbound CMEs and In Situ Comparison. Space Weather 16, 442. https://doi.org/10.1002/2017SW001767

Pizzo, V.: 1978, A three-dimensional model of corotating streams in the solar wind, 1. Theoretical foundations. J. Geophys. Res. Space Phys. 83, 5563. https://doi.org/10.1029/JA083iA12p05563

Press, W.H., Teukolsky, S.A., Vetterling, W.T., Flannery, B.P.: 1992, Numerical Recipes in C: The Art of Scientific Computing, 2nd edn. Cambridge University Press. ISBN 0521431085. Reiff, P.H.: 1990, The use and misuse of statistics in space physics. J. Geomag. Geoelec. 42, 1145 https://doi.org/10.5636/jgg.42.1145

Richardson, I.G., Cane, H.V.: 2012, Solar wind drivers of geomagnetic storms during more than four solar cycles. J. Space Weather Space Clim. 2, A01 https://doi.org/10.1051/swsc/2012001

Richardson, I.G., Cliver, E.W., Cane, H.V.: 2000, Sources of geomagnetic activity over the solar cycle: Relative importance of coronal mass ejections, high-speed streams, and slow solar wind. J. Geophys. Res. Space Phys. 105, 18203. https://doi.org/10.1029/1999JA000400

Richardson, I.G.: 2018, Solar wind stream interaction regions throughout the heliosphere. Liv. Rev. Solar Phys. 15, 1. https://doi.org/10.1007/s41116-017-0011-z

Richter, A.K., Luttrell, A.H.: 1986, Superposed epoch analysis of corotating interaction regions at 0.3 and 1.0 AU: A comparative study. J. Geophys. Res. Space Phys. 91, 5873. https://doi.org/10.1029/JA091iA05p05873

Russell, C.T., McPherron, R.L.: 1973, Semiannual variation of geomagnetic activity. J. Geophys. Res. 78, 92. https://doi.org/10.1029/JA078i001p00092

Sabine, E.: 1852, VIII. On periodical laws discoverable in the mean effects of the larger magnetic disturbance. 2014; No. II. Phil. Trans. Royal Society London 142, 103. https://doi.org/10.1098/rstl.1852.0009

Scargle, J.D., 1982. Studies in astronomical time series analysis. II-Statistical aspects of spectral analysis of unevenly spaced data. The Astrophysical Journal, 263, pp.835-853.

Schwabe, H.: 1844, Sonnen-Beobachtungen im Jahre 1843. Astronom. Nachr. 21, 233.

Sheeley Jr, N.R., Howard, R.A., Koomen, M.J. and Michels, D.J., 1983. Associations between coronal mass ejections and soft X-ray events. The Astrophysical Journal, 272, pp.349-354.

Sheeley, N.R., Asbridge, J.R., Bame, S.J., Harvey, J.W.: 1977, A pictorial comparison of interplanetary magnetic field polarity, solar wind speed, and geomagnetic disturbance index during the sunspot cycle. Solar Phys. 52, 485. https://doi.org/10.1007/BF00149663

Sheeley, N.R., Harvey, J.W.: 1981, Coronal holes, solar wind streams, and geomagnetic disturbances during 1978 and 1979. Solar Phys. 70, 237. https://doi.org/10.1007/BF00151331

Shelley, E.G., Johnson, R.G., Sharp, R.D.: 1972, Satellite observations of energetic heavy ions during a geomagnetic storm. J. Geophys. Res. 77, 6104. https://doi.org/10.1029/JA077i031p06104

Siscoe, G.L.: 1972, Structure and orientations of solar-wind interaction fronts: Pioneer 6. J. Geophys. Res. 77, 27. https://doi.org/10.1029/JA077i001p00027

Smith, E.J., Wolfe, J.H.: 1976, Observations of interaction regions and corotating shocks between one and five AU: Pioneers 10 and 11. Geophys. Res. Lett. 3, 137. https://doi.org/10.1029/GL003i003p00137

Smith, E.J., Wolfe, J.H.: 1976, Observations of interaction regions and corotating shocks between one and five AU: Pioneers 10 and 11. Geophys. Res. Lett. 3, 137. https://doi.org/10.1029/GL003i003p00137

Snyder, C.W., Neugebauer, M., Rao, U.R.: 1963, The solar wind velocity and its correlation with cosmic-ray variations and with solar and geomagnetic activity. J. Geophys. Res. 68, 6361. https://doi.org/10.1029/JZ068i024p06361

Souza, A.M., Echer, E., Bolzan, M.J.A. and Hajra, R., 2016. A study on the main periodicities in interplanetary magnetic field Bz component and geomagnetic AE index during HILDCAA events using wavelet analysis. Journal of Atmospheric and Solar-Terrestrial Physics, 149, pp.81-86. https://doi.org/10.1016/j.jastp.2016.09.006

Torrence, C. and Compo, G.P., 1998. A practical guide to wavelet analysis. Bulletin of the American Meteorological society, 79(1), pp.61-78 https://doi.org/10.1175/1520-0477(1998)079%3C0061:APGTWA%3E2.0.CO;2

Tranquille, C., Sanderson, T.R., Marsden, R.G., Wenzel, K.P. and Smith, E.J., 1987. Properties of a large-scale interplanetary loop structure as deduced from low-energy proton anisotropy and magnetic field measurements. Journal of Geophysical Research: Space Physics, 92(A1), pp.6-14.

Tsurutani, B.T., Gonzalez, W.D., Gonzalez, A.L., Tang, F., Arballo, J.K. and Okada, M., 1995. Interplanetary origin of geomagnetic activity in the declining phase of the solar cycle. Journal of Geophysical Research: Space Physics, 100(A11), pp.21717-21733.

Tsurutani, B.T., Gonzalez, W.D., Gonzalez, A.L.C., Guarnieri, F.L., Gopalswamy, N., Grande, M., Kamide, Y., Kasahara, Y., Lu, G., Mann, I., McPherron, R., Soraas, F., Vasyliunas, V.: 2006, Corotating solar wind streams and recurrent geomagnetic activity: A review. J. Geophys. Res. Space Phys. 111. https://doi.org/10.1029/2005JA011273

Tsurutani, B.T., Gonzalez, W.D., Gonzalez, A.L.C., Guarnieri, F.L., Gopalswamy, N., Grande, M., Kamide, Y., Kasahara, Y., Lu, G., Mann, I., McPherron, R., Soraas, F., Vasyliunas, V.: 2006, Corotating solar wind streams and recurrent geomagnetic activity: A review. J. Geophys. Res. Space Phys. 111. https://doi.org/10.1029/2005JA011273

Tsurutani, B.T., Gonzalez, W.D., Gonzalez, A.L.C., Guarnieri, F.L., Gopalswamy, N., Grande, M., Kamide, Y., Kasahara, Y., Lu, G., Mann, I., McPherron, R., Soraas, F., Vasyliunas, V.: 2006, Corotating solar wind streams and recurrent geomagnetic activity: A review. J. Geophys. Res. Space Phys. 111. https://doi.org/10.1029/2005JA011273

Tsurutani, B.T., Gonzalez, W.D., Tang, F., Akasofu, S.I. and Smith, E.J., 1988. Origin of interplanetary southward magnetic fields responsible for major magnetic storms near solar maximum (1978–1979). Journal of Geophysical Research: Space Physics, 93(A8), pp.8519-8531.

Tsurutani, B.T., Gonzalez, W.D., Tang, F., Akasofu, S.I., Smith, E.J.: 1988, Origin of interplanetary southward magnetic fields responsible for major magnetic storms near solar maximum (1978 – 1979). J. Geophys. Res. 93, 8519 https://doi.org/10.1029/JA093iA08p08519

Tsurutani, B.T., Gonzalez, W.D.: 1987, The cause of high-intensity long-duration continuous AE activity (HILDCAAs): Interplanetary Alfven wave trains. Planet. Space Sci. 35, 405. https://doi.org/10.1016/0032-0633(87)90097-3

Tsurutani, B.T., Gonzalez, W.D.: 1997, The Interplanetary Causes of Magnetic Storms: A562 Review, American Geophysical Union (AGU), 77. ISBN 9781118664612 https://doi.org/10.1029/GM098p0077

Tsurutani, B.T., Hajra, R., Echer, E., Gonzalez, W.D., Santolik, O.: 2016b, Predicting magnetospheric relativistic > 1 MeV electrons. NASA Tech Briefs 40, 20. http://www.techbriefs. com/component/content/article/ntb/tech-briefs/software/24815

Tsurutani, B.T., Hajra, R., Tanimori, T., Takada, A., Remya, B., Mannucci, A.J., Lakhina, G.S., Kozyra, J.U., Shiokawa, K., Lee, L.C., Echer, E., Reddy, R.V., Gonzalez, W.D.: 2016a, Heliospheric plasma sheet (HPS) impingement onto the magnetosphere as a cause of relativistic electron dropouts (REDs) via coherent EMIC wave scattering with possible consequences for climate change mechanisms. J. Geophys. Res. Space Phys. 121, 10130. https://doi.org/10.1002/2016JA022499

Tsurutani, B.T., Ho, C.M., Arballo, J.K., Goldstein, B.E., Balogh, A.: 1995, Large amplitude IMF fluctuations in corotating interaction regions: Ulysses at midlatitudes. Geophys. Res. Lett. 22, 3397. https://doi.org/10.1029/95GL03179

Tsurutani, B.T., Lakhina, G.S., Verkhoglyadova, O.P., Gonzalez, W.D., Echer, E., Guarnieri, F.L.: 2011, A review of interplanetary discontinuities and their geomagnetic effects. J. Atmos. Sol. Terr. Phys. 73, 5. https://doi.org/10.1016/j.jastp.2010.04.001

Tsurutani, B.T., Lin, R.P.: 1985, Acceleration of > 47 keV Ions and > 2 keV electrons by interplanetary shocks at 1 AU. J. Geophys. Res. 90, 1. https://doi.org/10.1029/JA090iA01p00001

VanderPlas, J.T., 2018. Understanding the lomb–scargle periodogram. The Astrophysical Journal Supplement Series, 236(1), p.16 http://dx.doi.org/10.3847/1538-4365/aab766

Wanliss, J.A., Showalter, K.M.: 2006, High-resolution global storm index: Dst versus SYM-H. J. Geophys. Res. Space Phys. 111, A02202. https://doi.org/10.1029/2005JA011034

Webb, D.F., Howard, R.A.: 1994, The solar cycle variation of coronal mass ejections and the solar wind mass ux. J. Geophys. Res. Space Phys. 99, 4201. https://doi.org/10.1029/93JA02742

Williams, D.J.: 1987, Ring current and radiation belts. Rev. Geophys. 25, 570. https://doi.org/10.1029/RG025i003p00570

Wilson, R.M., 1987. Geomagnetic response to magnetic clouds. Planetary and space science, 35(3), pp.329-335.

Wu, C.-C., Lepping, R.P.: 2016, Relationships Among Geomagnetic Storms, Interplanetary Shocks, Magnetic Clouds, and Sunspot Number During 1995 – 2012. Solar Phys. 291, 265 https://doi.org/10.1007/s11207-015-0806-9

Yurchyshyn, V., Hu, Q., Lepping, R.P., Lynch, B.J., Krall, J.: 2007, Orientations of LASCO Halo CMEs and their connection to the flux rope structure of interplanetary CMEs. Adv. Space Res. 40, 1821. https://doi.org/10.1016/j.asr.2007.01.059